UNIVERSITÀ DEGLI STUDI DI PADOVA

Dipartimento di Fisica e Astronomia "Galileo Galilei"

Master Degree in Astrophysics and Cosmology

Final dissertation

Nuclear statistical equilibrium in massive stars: investigating the influence of electron fraction

Thesis supervisor

Prof. Paola Marigo

Thesis co-supervisor

Dr. Michele Trabucchi

Thesis co-supervisor

Dr. Guglielmo Volpato

Candidate

Federico Mognol

Academic Year 2023/24

To my friends and loved ones, in any plane of existence.

Acknowledgements

I would like to thank my thesis supervisor, Prof. Paola Marigo, for inspiring me through the university years. I am also grateful to my co-supervisors, Dr. Michele Trabucchi and Dr. Guglielmo Volpato, for the help and guidance they gave me to complete this work. Finally, special thanks go to Dr. Franca Gava for the hardware assistance and overall support.

Contents

Abstract

The electron fraction is a key parameter characterizing the balance between nuclear reactions as well as weak processes in stellar interiors. It must be monitored carefully in stellar evolution calculations as it is of critical importance in stellar nucleosynthesis, especially in the late evolution of massive stars. Some recent studies highlighted the existence of uncertainties on this quantity. The present thesis represents an exploratory study of the impact of such uncertainty. The main goal is to characterize the influence of the electron fraction Y_e during the pre-supernova phase, assuming conditions of nuclear statistical equilibrium (NSE), under which the composition of the stellar core is determined only by temperature, density, and electron fraction. Employing the 1D stellar evolution code `MESA`, I determined these physical conditions for nine stellar models with different initial masses and then I computed the core abundances at NSE with `public_nse`, a tool specifically dedicated for this purpose. This allowed me to determine the total mass of ^{56}Ni, a representative isotope, contained in the core. I found that even small changes on the value of Y_e can lead to large uncertainties on this value, possibly greater than 100%. With a more structural oriented investigation, I determined also that an uncertainty of 1% on Y_e propagates as a $\sim 2\%$ uncertainty on the mass of the core. From this thesis I can argue that the uncertainty on Y_e can have important repercussions on the pre-supernova evolution of massive stars, in particular on the predicted abundances, the stability of the core and the explodability conditions.

Chapter 1

Nuclear physics

The stellar lifetime is characterized by the succession of many nuclear burnings. These are the source of energy that allows the star to maintain the hydrostatic equilibrium for much of its life and they feature a rich nucleosynthesis. In this chapter we discuss briefly some important quantities for the study of nuclear processes in stars.

1.1 Binding energy

The mass of the atomic nucleus m_{nuc} is less than the sum of the constituent nucleons and is given by

$$m_{nuc} = Zm_p + Nm_u - \Delta m \tag{1.1}$$

where m_p and m_n are the proton and neutron masses respectively. The quantity Δm instead is the *mass defect*, equivalent to an energy $\Delta E = \Delta mc^2$ which is referred to as *nuclear binding energy*. This constitutes the energy released in assembling a nucleus from its constituent nucleons through a nuclear fusion process or, equivalently, the energy required to separate the nucleus into its constituent nucleons. This binding energy can be written as

$$B(Z, N) = (Zm_p + Nm_p - m_{nuc})c^2 \tag{1.2}$$

Nuclear processes liberate energy as long as the binding energy per nucleon $B(Z, A)/A$ of the products exceeds that of the initial constituents. The largest values of binding energy per nucleon are encountered in the iron peak nuclides, characterized by mass numbers $A = 50 - 65$. This means that energy can be liberated either by the fusion of nuclei lighter than iron or by the fission of heavier ones.

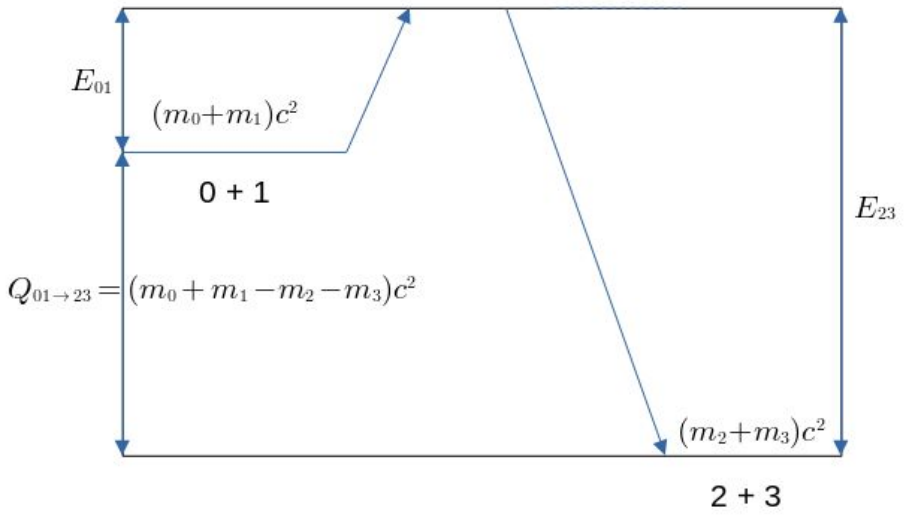

Figure 1.1: General reaction where all species are massive particles.

1.2 Energetics of nuclear reactions

A nuclear interaction can be written as $0+1 \longrightarrow 2+3$ or $0(1,2)3$, where 0 and 1 are the nuclei before the interaction, and 2 and 3 are the interaction products. We can have a radiative capture reaction if 2 is a photon or a photodisintegration if 1 is a photon instead. To illustrate the energetics of nuclear reactions, energy level diagrams (Figs. 1.1 and 1.2) can be used. These diagrams contain the colliding species on the left hand side, called entrance channel, and the products on the right, the exit channel. The vertical direction represents the energy scale. The energy conservation imposes that

$$m_0c^2 + m_1c^2 + E_0 + E_1 = m_2c^2 + m_3c^2 + E_2 + E_3 \tag{1.3}$$

where the m_i are the rest masses and E_i the kinetic energies of the nuclei. The condition can be written also as

$$Q_{01\to 23} = m_0c^2 + m_1c^2 - m_2c^2 - m_3c^2 = E_0 + E_1 - E_2 - E_3 \tag{1.4}$$

The quantity Q is the Q-value of the reaction, representing the difference in rest masses before and after the reaction: if $Q > 0$ the reaction is exothermic, if $Q < 0$ it is endothermic. The composition of the stellar plasma is characterized by several important quantities. The number density of nuclei N_i is equal to the total number of species i per unit volume, so the mass density can be written as $\rho = N_i m_i = (1/N_A)\sum_i N_i M_i$ where N_A is the Avogadro's number. Then we can now write

$$\frac{\sum_i N_i M_i}{\rho N_A} = \frac{N_1 M_1}{\rho N_A} + \frac{N_2 M_2}{\rho N_A} + \cdots = X_1 + X_2 + \cdots = \sum_i X_i = 1 \tag{1.5}$$

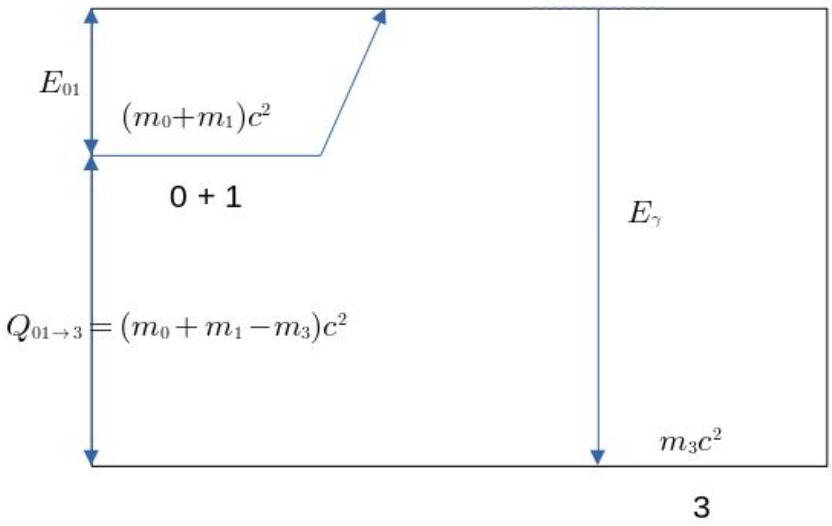

Figure 1.2: General reaction where there are both massive and massless particles.

where $X_i \equiv \frac{N_i M_i}{\rho N_A}$ is the mass fraction, the fraction of mass bounded to species i. A related quantity is the mole fraction, defined as $Y_i \equiv \frac{X_i}{M_i} = \frac{N_i}{\rho N_A}$, which is useful as it changes only due to nuclear reactions and it is constant against changes in ρ caused by the expansion or compression of the stellar plasma, while N_i instead depends on ρ. It must be noted that, even without expansion or compression, ρ is not a conserved quantity, due to the nuclear reactions transforming a small fraction of mass into energy or leptons. For this reason, it is better to work with mass number A_i rather than with relative mass M_i. With this new quantity we can define the nucleon density ρ_A as

$$\rho_A = (1/N_A) \sum_i N_i A_i \tag{1.6}$$

and the nucleon fraction X_i as

$$X_i = N_i A_i / (\rho_a N_A) \tag{1.7}$$

These quantities are conserved under nuclear transformations, therefore they can be used instead of the mass density and the mass fraction, respectively. The number density evolution of an unstable nuclide is given by the differential equation

$$\left(\frac{dN}{dt}\right) = -\lambda N \tag{1.8}$$

where λ is the decay constant, representing the probability of decay per nucleus per time, that, as the name suggests, is constant under the conditions of con-

stant temperature and density. Integrating this equation, one can obtain the radioactive decay law for the number density of nuclei remaining after a time t

$$N = N_0 e^{-\lambda t} \tag{1.9}$$

where N_0 is the initial number density at $t = 0$. The time needed for the number density to reach one-half of its initial abundance, $N_0/2 = N_0 e^{-\lambda T_{1/2}}$ is called half-life $T_{1/2}$, with

$$T_{1/2} = \frac{\ln 2}{\lambda} = \frac{0.69315}{\lambda} \tag{1.10}$$

Another timescale is the mean lifetime τ, the time it takes for N to fall to $1/e = 0.36788$ of the initial abundance, $N_0/e = N_0 e^{-\lambda \tau}$, which is given by

$$\tau = \frac{1}{\lambda} = 1.4427 T_{1/2} \tag{1.11}$$

Some nuclides can undergo different competing decays, so the total decay probability is given by the sum of the probabilities of the individual processes, so

$$\lambda = \sum_i \lambda_i \tag{1.12}$$

is the total decay probability, where λ_i is the partial decay constant. Multiplying the decay constant with the total number of nuclei $\mathcal{N}$, determines the total number of decays per unit time, a quantity that is referred to as the activity $A \equiv \lambda \mathcal{N} = -d\mathcal{N}/dt$, measured in curie and becquerel. Stable nuclides are not radioactive and so do not spontaneously undergo radioactive decay. The stability of isotopes is affected by the ratio of protons to neutrons and by the presence of *magic numbers* of neutrons and protons, corresponding to major shell closures in the nuclear shell model. These numbers are 2, 8, 20, 28, 50, 82 and 126. Some nuclides, such as helium, oxygen, calcium, nickel, tin and lead, have both a magic number of protons and neutrons. For this reason they are called *double magic* and they are particularly stable against decay.

1.3 Weak interaction processes

The energy generation of nuclear reactions and the resulting nucleosynthesis are governed by the strong and the electromagnetic forces. Besides them, also the weak interaction plays an important role. In fact, when a nuclide is produced in a nuclear burning, its decay via weak-interaction processes will compete with its destruction due to nuclear reactions. Moreover, the weak interaction determines the neutron excess parameter η during the nucleosynthesis, expressed as

$$\eta = \sum_i (N_i - Z_i) Y_i = \sum_i \frac{(N_i - Z_i)}{M_i} X_i \tag{1.13}$$

with $-1 \leq \eta \leq 1$. The quantities N_i, Z_i, M_i, Y_i and X_i refer to the number of neutrons, the number of protons, the relative atomic mass, the mole fraction

and the mass fraction, respectively, and the sum runs over all the i nuclides present in the plasma. The neutron excess parameter can change only due to weak interactions and so it is important to monitor this quantity for many reasons. First, it is crucial in the nucleosynthesis during the late burning stages in massive stars and during explosive burning. Second, the electron capture affects the stability conditions of the degenerate iron core before a supernova explosion, as it reduces the number of electrons available for support through degenerate pressure. Third, the neutrinos emitted in weak interactions affect the energy budget of stars and thus their evolution and explosion mechanism. A closely related quantity is the electron fraction Y_e, defined as $Y_e = \frac{N_e}{\sum_i N_i M_i}$ with N_e being the electron number density. From this equation, we can see that Y_e is related to η by $\eta = 1 - 2Y_e$. This quantity will be treated further in the following chapters.

The β-decay is a type of radioactive decay in which an atomic nucleus emits a *beta* particle (an electron or a positron) and becomes an isobar of that nuclide. A simple example is given by the decay of the free neutron into a proton through the reaction

$$\mathrm{n} \longrightarrow \mathrm{p} + \mathrm{e}^- + \bar{\nu} \tag{1.14}$$

with e^- and $\bar{\nu}$ being the electron and antineutrino respectively. The half-life of the free neutron amounts to $T_{1/2} = 10.2\,\mathrm{min}$, making this decay slower by many orders of magnitude compared to the typical nuclear reaction timescales or the electromagnetic decay probability: the interaction causing the β-decay must be very weak. The most common weak interaction processes in nuclear β-decay are

$$\begin{aligned}
{}^{\mathrm{A}}_{\mathrm{Z}}\mathrm{X}_{\mathrm{N}} &\longrightarrow {}^{\mathrm{A}}_{\mathrm{Z+1}}\mathrm{X'}_{\mathrm{N-1}} + \mathrm{e}^- + \bar{\nu} && \beta^-\text{- decay (electron emission)} && (1.15a)\\
{}^{\mathrm{A}}_{\mathrm{Z}}\mathrm{X}_{\mathrm{N}} &\longrightarrow {}^{\mathrm{A}}_{\mathrm{Z-1}}\mathrm{X'}_{\mathrm{N+1}} + \mathrm{e}^+ + \nu && \beta^+\text{- decay (positron emission)} && (1.15b)\\
{}^{\mathrm{A}}_{\mathrm{Z}}\mathrm{X}_{\mathrm{N}} + \mathrm{e}^- &\longrightarrow {}^{\mathrm{A}}_{\mathrm{Z-1}}\mathrm{X'}_{\mathrm{N+1}} + \nu && \text{electron capture} && (1.15c)\\
{}^{\mathrm{A}}_{\mathrm{Z}}\mathrm{X}_{\mathrm{N}} + \nu &\longrightarrow {}^{\mathrm{A}}_{\mathrm{Z+1}}\mathrm{X'}_{\mathrm{N-1}} + \mathrm{e}^- && \text{neutrino capture} && (1.15d)\\
{}^{\mathrm{A}}_{\mathrm{Z}}\mathrm{X}_{\mathrm{N}} + \bar{\nu} &\longrightarrow {}^{\mathrm{A}}_{\mathrm{Z-1}}\mathrm{X'}_{\mathrm{N+1}} + \mathrm{e}^+ && && (1.15e)
\end{aligned}$$

where e^+, ν and $\bar{\nu}$ are the positron, neutrino and antineutrino respectively. These interactions changes the chemical identity of the nuclide, but the mass number A remains the same. The energy released in the β-decay is given by the difference in atomic masses before and after the interaction, therefore

$$\begin{aligned}
Q_{\beta-} &= [m({}^{\mathrm{A}}_{\mathrm{Z}}\mathrm{X}_{\mathrm{N}}) - m({}^{\mathrm{A}}_{\mathrm{Z+1}}\mathrm{X'}_{\mathrm{N-1}})]c^2 && \beta^-\text{-decay} && (1.16a)\\
Q_{e^+} &= [m({}^{\mathrm{A}}_{\mathrm{Z}}\mathrm{X}_{\mathrm{N}}) - m({}^{\mathrm{A}}_{\mathrm{Z-1}}\mathrm{X'}_{\mathrm{N+1}}) - 2m_e]c^2 && \text{positron emission} && (1.16b)\\
Q_{EC} &= [m({}^{\mathrm{A}}_{\mathrm{Z}}\mathrm{X}_{\mathrm{N}}) - m({}^{\mathrm{A}}_{\mathrm{Z-11}}\mathrm{X'}_{\mathrm{N+1}})]c^2 - E_b && \text{electron capture} && (1.16c)
\end{aligned}$$

with m_e being the electron mass and E_b the atomic binding energy of the captured electron. The emitted energy is almost entirely transferred to the emitted leptons. It must be noted that for positron emission in a stellar plasma, the energy release calculated from the mass difference of parent and daughter nucleus

alone, $Q'_{e^+} = [m(^{\mathrm{A}}_{\mathrm{Z}}\mathrm{X}_{\mathrm{N}} - \mathrm{m}(_{\mathrm{Z}-1}{}^{\mathrm{A}}\mathrm{X}'_{\mathrm{N}+1}))]c^2$ accounts also for the annihilation of the positron with an electron of the environment, given by $2m_e c^2 = 1022\,\mathrm{keV}$, so this quantity is more useful than Q_{e^+} when calculating positron emission energy release. For what concerns the neutrinos released in nuclear β-decay, these leptons interact so weakly with matter that they escape freely from the stellar plasma, unless the density ρ is very high ($\rho \geq 10^{11}\,\mathrm{g\,cm^{-3}}$). This means that, when computing the energy budget of a star, the neutrino energy must be subtracted from the total energy liberated. During the later stages of stellar evolution, neutrinos become important for the transport of energy from the interior to the surface. In fact, at very high temperatures ($T > 10^9\,\mathrm{K}$) a conspicuous number of photons have energy in excess of the pair production threshold, leading to the production of an electron-positron pair $\gamma \longrightarrow \mathrm{e}^- + \mathrm{e}^+$ that subsequently may annihilate via the reaction $\mathrm{e}^- + \mathrm{e}^+ \longrightarrow 2\,\gamma$ or the reaction $\mathrm{e}^- + \mathrm{e}^+ \longrightarrow \nu + \bar{\nu}$. The produced neutrinos escape freely from the star and they represent the main energy loss mechanism during later stages of stellar lifetime. This energy loss can be determined directly from the neutrino production rate and represents the main cause of the short lifetimes of later burnings.

Chapter 2

Stellar evolution

2.1 Star formation and evolution

Stars are born from the gravitational collapse of a molecular cloud. As the cloud contracts, gravitational potential energy is transformed into thermal energy and radiation. Initially, the gas is in free fall and most of the energy is not retained by the object, but radiated away because the gas is still relatively transparent. As the density increases so does the opacity and some of the emitted radiation starts to be absorbed in the cloud. Now the temperature and pressure begin to rise, slowing down the contraction of the inner part of the cloud. The increasing temperature dissociate hydrogen molecules into atoms then it ionizes hydrogen and helium atoms. When a temperature of about $10^5\,K$ is reached the gas is almost completely ionized: electrons trap the radiation efficiently and as a result pressure and temperature increase, halting the collapse of the central part of the cloud. The pre-main sequence star eventually reaches hydrostatic equilibrium while still accreting mass from the cloud. During this stage the source of energy is gravitational contraction. When the internal temperature reaches a few million Kelvin, the first nuclear reactions start to occur with the deuterium burning. However, is only when the temperature rises to about $10^7\,K$ that the fusion of hydrogen starts to occur: the star reaches thermal equilibrium and it is now at the zero age main sequence (ZAMS). The fate of the star depends on its initial mass, the one it has when it reaches the ZAMS. The evolution of massive stars, those with masses $M \geq 11 M_\odot$, is relatively short and their total life amounts only to $\approx 7\,Myr$ for a $25\,M_\odot$ star. The star spends about 90% of this time in the main-sequence, burning hydrogen through the CNO cycle in the core. When hydrogen is exhausted in the center, the burning shifts to a shell. The core contracts and heats up until helium is ignited. This new burning heats up also the hydrogen burning shell and the outer layers of the star expands greatly. The star is now a supergiant, in which the helium burning in the core will continue for about 8×10^5 years. When also the helium is depleted in the core, the He-burning shifts to a shell located just below the hydrogen burning

one. The peculiarity of massive stars is their capability of starting successive burning stages in their core, using as a fuel the ashes left by the previous one. These are referred to as *carbon burning*, *neon burning*, *oxygen burning* and *silicon burning*, and are collectively referred to as *advanced burning stages*. The fundamental difference between the initial burning stages and the advanced ones is in the manner by which the nuclear energy produced in the interior is radiated from the surface. While for H and He burnings the energy is almost exclusively radiated as light, during the advanced stages light represents only a small fraction and most of the energy is transported by neutrino-antineutrino pairs. This contribution increases during the advanced stages, accelerating the evolution of the star: Si-burning, for example, lasts for about 1 day. Such a rapid evolution of the interior cannot be followed by the envelope, which remains unchanged. Therefore, the star after C-burning occupies the same position in the H-R diagram for the rest of its life. After Si exhaustion, the structure of the core consists of several layers of different composition, separated by thin nuclear burning shells. The stellar core at this point is degenerate and has no other sources of nuclear energy, as it is composed mostly by iron. The core continues to grow in mass due to the ashes produced by the burnings in the overlying shells. At some point, it will reach the Chandrasekhar mass limit of $\approx 1.44 M_{\odot}$, at which the electron degeneracy is no more able to counteract gravity, leading to the collapse of the core in a free-fall timescale.

2.2 Thermonuclear reactions in stars

Nuclear reactions in the interior of stars give rise to the necessary internal pressure that prevents their gravitational collapse. This condition is what defines the hydrostatic equilibrium, in which the gravitational force is equal to the internal pressure and is maintained by all stable stars. Moreover, nuclear reactions synthesize all the chemical elements that weren't produced in the primordial nucleosynthesis, enriching the interstellar medium with elements that, ultimately, make possible also the development of life. In the next sections we'll discuss briefly each burning stage, with a particular focus on the Si-burning one, since it is of outmost importance for this thesis.

2.2.1 Cross sections and reaction rates

In the first chapter we have seen that the energy released by a particular nuclear reaction is represented by the Q-value. However, what is important in a stellar environment is the energy liberated per unit volume, that depends on the nuclear cross section and the velocity distribution of particles in the plasma. The nuclear cross section, usually denoted as σ, represents the probability that a nuclear reaction will occur between a pair of interacting nuclei 0 and 1. Let's suppose that a beam of N_b particles per unit time t, covering an area A, is incident on a target and the non-overlapping target nuclei within the beam are N_t. We assume that the total number of interactions that occur per unit time, N_R/t, is equal

to the total number of emitted reaction products per unit time, N_e/t. If the interaction products are scattered incident particles, we are referring to elastic scattering, if they are different particles, then we are referring to a reaction. The number of interaction products emitted at an angle θ with respect to the beam direction into the solid angle $d\Omega$, is defined as $N_e^{d\Omega}$. The area perpendicular to the direction θ covered by a radiation detector is given by $dF = r^2 d\Omega$. The cross section is defined as

$$\begin{aligned}\sigma \equiv \frac{\left(\text{number of interactions per time}\right)}{\left(\text{number of incident particles per area per time}\right)\left(\text{number of target nuclei within the beam}\right)} = \\ = \frac{(N_R/t)}{[N_b/(tA)]N_t}\end{aligned} \tag{2.1}$$

Commonly, the nuclear cross section σ is expressed with *barns* (b), where $1\,\mathrm{b} \equiv 10^{-28}\,\mathrm{m}^2$. In general, nuclear cross sections depend on the relative velocity of the target-projectile system, so it is a function $\sigma = \sigma(v)$. Using the equation 2.1, the nuclear reaction rate (representing the number of reactions per time t and unit volume V) can be written as

$$\frac{N_R}{V \times t} = (\sigma N_t)\left(\frac{N_b}{V \times A \times t}\right) = \sigma \frac{N_t}{V}\frac{N_b}{A \times t} = \sigma \frac{N_t}{V} v \frac{N_b}{V} \tag{2.2}$$

with $j_b = N_b/(At) = vN_b/V$ being the current density (the number of particles per time per area). If we consider now a reaction involving four species, $0+1 \rightarrow 2+3$, in which both 0 and 1 are particles with rest mass, the reaction rate of eq. 2.2 can be rewritten as

$$r_{01} = N_0 N_1 v \sigma(v) \tag{2.3}$$

where $N_0 \equiv N_t/V$ and $N_1 \equiv N_b/V$ are the number densities of the interacting particles. Since the relative velocity v of the particles is not constant, but there is a distribution of velocities defined by the probability distribution function $P(v)$, the reaction rate can be generalized as

$$r_{01} = N_0 N_1 \int_0^\infty v P(v) \sigma(v) dv \equiv N_0 N_1 \langle \sigma v \rangle_{01}. \tag{2.4}$$

Taking into account also the reactions between identical particles with the Kronecker symbol δ_{01}, we obtain the general expression

$$r_{01} = \frac{N_0 N_1 \langle \sigma v \rangle_{01}}{(1+\delta_{01})}. \tag{2.5}$$

In most cases the particles are not relativistic and non degenerate, so their velocities can be described as a Maxwell-Boltzmann distribution, and this applies also to their relative velocities. This means we can write the probability distribution function as

$$P(v)dv = \left(\frac{m_{01}}{2\pi kT}\right)^{3/2} e^{-m_{01}v^2/(2kT)} 4\pi v^2 dv \tag{2.6}$$

which gives the probability that the relative velocity is between v and $v + dv$. Another important reaction, especially during the later stages, is the photodisintegration reaction $\gamma + 3 \rightarrow 0 + 1$, where γ is a photon. In this case the reaction rate can be written as

$$r_{\gamma 3} = N_3 N_\gamma c \sigma(E_\gamma) \tag{2.7}$$

the cross section σ here depends on the γ-ray energy (E_γ) and the number density of photons depends on temperature and E_γ, so it can be generalized as

$$r_{\gamma 3} = N_3 \int_0^\infty c N_\gamma(E_\gamma) \sigma(E_\gamma) dE_\gamma \tag{2.8}$$

2.2.2 Abundance evolution

To study how the abundances of the various species evolve with time, let's consider first a reaction between two nuclei 0 and 1. The rate of change of nucleus 0 due to the reactions with 1 is given by

$$\left(\frac{dN_0}{dt}\right)_1 = -\lambda_1(0) N_0 = -\frac{N_0}{\tau_1(0)} \tag{2.9}$$

where $\lambda \equiv 1/\tau$ is the decay constant we have defined in the previous chapter and $\tau_1(0)$ is the lifetime of the 0 nucleus against the reaction with 1. Using the reaction rate of eq. 2.5 we can also write

$$\begin{aligned} \left(\frac{dN_0}{dt}\right)_1 &= -(1+\delta_{01}) r_{01} = -(1+\delta_{01}) \frac{N_0 N_1 \langle \sigma v \rangle_{01}}{(1+\delta_{01})} = \\ &= -N_0 N_1 \langle \sigma v \rangle_{01} \end{aligned} \tag{2.10}$$

in which appears the Kronecker symbol, as for identical nuclei each reaction destroys two particles. In general, the species 0 can be destroyed by different reactions, so its total lifetime is given by

$$\frac{1}{\tau(0)} = \sum_i \frac{1}{\tau_i(0)} \tag{2.11}$$

In general, if we neglect other factors as expansion or mixing and the only sources of abundance change are the nuclear processes, the abundance evolution of a nucleus i can be expressed with the differential equation

$$\begin{aligned} \frac{dN_i}{dt} = &\left[\sum_{j,k} N_j N_k \langle \sigma v \rangle_{jk \rightarrow i} + \sum_l \lambda_{\beta, l \rightarrow i} N_l + \sum_m \lambda_{\gamma, m \rightarrow i} N_m \right] + \\ &- \left[\sum_n N_n N_i \langle \sigma v \rangle_{ni} + \sum_o \lambda_{\beta, i \rightarrow o} N_i + \sum_p \lambda_{\gamma, i \rightarrow p} N_i \right] \end{aligned} \tag{2.12}$$

The terms in the first parenthesis are the production processes leading to the formation of nucleus i: the first term is the sum over all the reaction between

j and k nuclei that produce i, the second one is the sum over all the β-decays of nuclei l leading to i and the third is the sum over all photodisintegration reactions of nuclei m that produces i. Similarly, in the other parenthesis there are the destruction processes involving nucleus i. If a reaction between non identical particles produces two nuclei, then $N_j N_k \langle \sigma v \rangle_{jk \to i}$ must be replaced by $2N_j N_k \langle \sigma v \rangle_{jk \to i}$. If a reaction between identical particles ($j = k$) produces only one particle, then $N_j N_k \langle \sigma v \rangle_{jk \to i}$ must be replaced by $N_j^2 \langle \sigma v \rangle_{jj \to i}/2$. If the mass density changes during the nucleosynthesis it is preferable to express the eq 2.12 in terms of mole fraction Y instead of number density N, since Y do not depends on density and so it is not affected by the expansion or compression of the gas.

The above treatment considers the evolution of only one species, but in a realistic situation we have to deal with many nuclides simultaneously, each of them with an abundance evolution described by eq 2.12. What we get is a system of coupled non-linear ordinary differential equations called *nuclear reaction network*, that in most cases must be solved numerically. Particular conditions may lead to fundamental properties, with the most important being the *steady state* and *equilibrium*. A steady state solution exists if for some part of the reaction network the time derivative of all abundances is equal or close to 0, so $dN_i/dt \sim 0$, meaning that the sum of all production terms is balanced by the destruction ones. In this case the abundances are constant. An equilibrium solution is more restrictive and it applies if the abundances of a group of nuclei are locally balanced due to the forward and reverse reaction rates being almost equal. In this case abundances are not constant.

2.3 Nuclear burning stages

For a given temperature and composition, the reactions with the smallest Coulomb barriers will proceed faster and will account for most of the energy generation in the stellar core. Hydrogen and helium are by far the most abundant elements in the stellar plasma and also the ones with the smallest Coulomb barriers, therefore we expect nuclear reactions involving them as the main energy source in most stars.

2.3.1 Hydrostatic H-burning

The first nuclear burning stage is represented by H-burning. This process releases the most energy per unit mass among all the burning stages ($\approx 6 \times 10^{24} Mev/g$). Thus, this fuel is consumed more slowly than the others during the stellar lifetime, making this stage (corresponding to the main sequence) the longest one. This process consists on the fusion of four ^{1}H nuclei to form ^{4}He with the release of an energy $Q = 26.71 MeV$. However, the simultaneous interaction of four protons in the stellar plasma is very unlikely. There are other mechanisms, involving the interaction of two protons in the entrance channel, that are more likely to occur. In particular, the dominant mechanisms

are represented by the *proton-proton (pp) chains* and the *CNO cycles*. There are three main pp-chains: the pp1, pp2 and pp3. The dominant one depends on the temperature. In general, the pp1 chain generates most of the energy below $T \approx 18MK$, between $T \approx 18MK$ and $T \approx 25MK$ the pp2 and above $T \approx 25MK$ the pp3. This means that for larger mass stars, composed exclusively of H and He, pp3 should be the dominant pp chain reaction. However, most stars contain also heavier nuclides, in particular C, N and O, that can participate in the H-burning. These conditions produce four sets of reactions collectively called CNO cycles. This family of reactions produce the same result of the pp chain, with the heavier nuclei acting only as catalysts, which means that their total abundance is not altered in the process. The equilibrium energy generation of pp chain and CNO cycles depends on temperature T, but the relation is steeper for the CNO making this process the dominant one for $T > 20\,MK$(i.e. in higher mass stars). This different dependence on temperature affects also the internal structure of stars: while in low-mass stars, where helium is synthesized mainly by pp chain, the energy transport from the core is radiative, in massive stars convection is the primary transport mechanism.

2.3.2 He-burning

At the end of the core H-burning, this process shifts to a shell. The core now consists mostly of He and it contracts until this new fuel is ignited at a temperature $T \approx 1.5 \times 10^8 K$. The He-burning starts with the 3α reaction, that represents a two step process. In the first, two α particles interact to form ^{8}Be in its ground state. This particle is unstable at relatively low temperatures and disintegrates back to two α with a half-life $T_{1/2} = 8.2 \times 10^{-17}\,s$, but a small concentration of ^{8}Be will eventually build up until its rate of formation balances the decay one, so

$$^4\mathrm{He} + {}^4\mathrm{He} \longleftrightarrow {}^8\mathrm{Be} \tag{2.13}$$

In the second step, a α-particle interacts with ^{8}Be to form ^{12}C through $^8\mathrm{Be}(\alpha,\gamma)^{12}\mathrm{C}$ reaction, that proceeds via an excited state in ^{12}C. During hydrostatic He-burning a rich nucleosynthesis takes place: as He abundance decreases, the α particle captures on ^{12}C become increasingly important, leading to the production of ^{16}O, ^{20}Ne and ^{24}Mg. Initially, the 3α reaction increases the ^{12}C abundance until it reaches a maximum. Then the α captures on ^{12}C become increasingly important and the ^{16}O abundance rises, eventually surpassing the ^{12}C abundance. This reaction, $^{12}\mathrm{C}(\alpha,\gamma)^{16}\mathrm{O}$, produces about one third of the total energy during the hydrostatic helium burning, with the rest produced by the 3α. The end products of He-burning are mainly ^{12}C and ^{16}O, with their abundance ratio depending on the burning T and ρ (i.e. the stellar mass). For larger mass stars we expect more ^{16}O production with respect to ^{12}C. The He-burning phase in massive stars is characterized also by the reaction

$$^{14}\mathrm{N}(\alpha,\gamma)\,{}^{18}\mathrm{F}(\beta^+\,\nu)\,{}^{18}\mathrm{O}(\alpha,\gamma)\,{}^{22}\mathrm{Ne} \tag{2.14}$$

which is the main source of ^{22}Ne in the universe, and by the $^{22}\mathrm{Ne}(\alpha,\mathrm{n})\,^{25}\mathrm{Mg}$ reaction. This latter has a negative Q-value and is rather slow, but near the end of He-burning it becomes an important source of neutrons that affects the synthesis of neutron-rich nuclides in the $A = 60 - 90$ range and the neutron excess parameter η during the core He burning.

2.3.3 C-burning

When He is exhausted in the center of the star, the core starts a new contraction phase and the temperature rises until the next fuel is ignited. At this point the core is composed mostly of ^{12}C and ^{16}O. Among those involving these two species, the fusion of two ^{12}C nuclei is the reaction with the lowest Coulomb barrier and so it initiates the next burning stage, the so called carbon burning. This process produces ^{24}Mg in a highly excited state, which decays preferentially with the emission of p, n and α-particles through the reactions

$$^{12}\mathrm{C}(^{12}\mathrm{C},\mathrm{p})^{23}\mathrm{Na} \qquad (Q = 2241\,KeV) \tag{2.15a}$$

$$^{12}\mathrm{C}(^{12}\mathrm{C},\alpha)^{20}\mathrm{Ne} \qquad (Q = 4617\,KeV) \tag{2.15b}$$

$$^{12}\mathrm{C}(^{12}\mathrm{C},\mathrm{n})^{23}\mathrm{Mg} \qquad (Q = -2599\,KeV) \tag{2.15c}$$

The liberated particles can be consumed quickly by secondary reactions involving ^{12}C, ^{16}O, ^{23}Na and ^{20}Ne. Therefore, the carbon burning indicates not only the fusion of two carbon nuclei, but this complex network of primary and secondary reactions. Depending on star mass, this process takes place at temperatures $T = 0.6 - 1.0\,GK$ and its fusion cross section is dominated by the p and α channels of reactions 2.15a and 2.15b respectively. In fact, the branching ratios amount to $B_p \approx B_\alpha = (1 - B_n)/2$, where B_n is a small number, usually $B_n = 2 - 10\%$, but declines rapidly for lower T: the reaction rate of 2.15c is by far the smallest one. The calculation performed on a $25\,M_\odot$ core carbon burning star model with solar metallicity shows that, while most of the ^{12}C fuel is consumed, nearly all of the initial abundance of ^{16}O is conserved at the end of the calculation. Also the ^{22}Ne declines, but many other species increase their abundances. With progressing time, the number of liberated protons and α particles also declines and the nucleosynthesis involving their capture slows down. At the end of carbon burning the most abundant nuclides are ^{16}O, ^{20}Ne, ^{24}Mg and ^{23}Na.

2.3.4 Ne-burning

Ne-burning starts when most of the ^{12}C is exhausted and the core starts contracting gravitationally increasing both its temperature and density. When the temperature rises to values $T > 1\,GK$, photodisintegration processes become important. The n, p and α separation energies of ^{16}O, ^{23}Na and ^{24}Mg are quite

high ($\approx 7-17\,MeV$) even at these temperature ranges, but this is not the case for ^{20}Ne. This nucleus has a rather low α separation energy of $4.73\,MeV$. The result is that the decay constant at $T = 1.5\,GK$ is $\lambda_\gamma(^{20}\mathrm{Ne}) = 1.5 \times 10^{-6}\,s^{-1}$ and so ^{20}Ne will photodisintegrate. The liberated α particles can in turn participate in other reactions, like being captured by ^{16}O to produce again ^{20}Ne. The neon burning consists of the primary reaction

$$^{20}\mathrm{Ne}(\gamma,\alpha)^{16}\mathrm{O} \qquad (Q = -4730\,KeV) \tag{2.16}$$

and the secondary reactions

$$^{20}\mathrm{Ne}(\alpha,\gamma)^{24}\mathrm{Mg}(\alpha,\gamma)^{28}\mathrm{Si} \qquad (Q_{^{20}\mathrm{Ne}(\alpha,\gamma)} = 9316\,KeV) \tag{2.17a}$$

$$(Q_{^{24}\mathrm{Mg}(\alpha,\gamma)} = 9984\,KeV) \tag{2.17b}$$

$$^{23}\mathrm{Na}(\alpha,\mathrm{p})^{26}\mathrm{Mg}(\alpha,\mathrm{n})^{29}\mathrm{Si} \qquad (Q_{^{23}\mathrm{Na}(\alpha,\mathrm{p})} = 1821\,KeV) \tag{2.17c}$$

$$(Q_{^{26}\mathrm{Mg}(\alpha,\mathrm{n})} = 34\,KeV) \tag{2.17d}$$

The primary reaction is endothermic, but the combination with the secondary reactions gives a net production of energy. The temperatures during Ne-burning are in the range $T = 1.2-1.8\,GK$ and the calculations performed at $T \approx 1.5\,GK$ show that the energy generation rate scales like $\epsilon_{Ne}(T) \propto T^{49}$ and the energy liberated by each $^{20}\mathrm{Ne} + {}^{20}\mathrm{Ne}$ conversion is on average $Q \approx 6.2\,MeV$. While ^{20}Ne is gradually consumed, the abundance of ^{16}O increases with time. At the end of the Ne-burning the core contains mainly ^{16}O, ^{24}Mg and ^{28}Si.

2.3.5 O-burning

After the exhaustion of Ne, the core enters a new contraction phase. The temperature increases until the next fuel is ignited. The most likely reaction induced by the combination of the nuclides found at the end of Ne-burning is the $^{16}\mathrm{O} + {}^{16}\mathrm{O}$ fusion reaction, since it has the lowest Coulomb barrier. The nucleus formed by this process is the highly excited ^{32}S, that will eventually decay with the emission of light particles, so the situation is similar to C-burning. However, as this compound nucleus has a much higher excitation energy ($E \approx 16.5\,MeV$), the possible exit channels are more varied. Some of the most important primary reactions include

$$^{16}\mathrm{O}(^{16}\mathrm{O},\mathrm{p})^{31}\mathrm{P} \qquad (Q = 7678\,KeV) \tag{2.18a}$$

$$^{16}\mathrm{O}(^{16}\mathrm{O},2\,\mathrm{p})^{30}\mathrm{Si} \qquad (Q = 381\,KeV) \tag{2.18b}$$

$$^{16}\mathrm{O}(^{16}\mathrm{O},\alpha)^{28}\mathrm{Si} \qquad (Q = 9594\,KeV) \tag{2.18c}$$

$$^{16}\mathrm{O}(^{16}\mathrm{O},2\,\alpha)^{24}\mathrm{Mg} \qquad (Q = -390\,KeV) \tag{2.18d}$$

$$^{16}\mathrm{O}(^{16}\mathrm{O}\,,\mathrm{d})^{30}\mathrm{P} \qquad (Q = -2409\,KeV) \tag{2.18e}$$

$$^{16}\mathrm{O}(^{16}\mathrm{O},\mathrm{n})^{31}\mathrm{S} \qquad (Q = 1499\,KeV) \tag{2.18f}$$

The liberated particles then participate in many secondary reactions involving the heavy products of primary reactions and also the ashes left by Ne-burning. This combination of primary and secondary reactions constitutes the O-burning. The typical temperatures during this phase are in the range $T = 1.5 - 2.7\,\mathrm{GK}$. For what concerns reaction rates, the protons emission channel dominates at all temperatures with a contribution of $\approx 62\%$ at $T = 2.2\,GK$, followed by the α particle and neutrons ones. Similar to C-burning, the secondary reactions contribute significantly to the nuclear energy generation. At $T = 2.2\,GK$ the average energy release is $Q = 17.2\,MeV$ for each $^{16}\mathrm{O} + {}^{16}\mathrm{O}$ reaction with an energy generation rate that scales as $\epsilon(T) \propto T^{34}$. As the O-burning proceeds, $^{16}\mathrm{O}$ is quickly depleted in less than a year and the abundances of $^{28}\mathrm{Si}$ and $^{32}\mathrm{S}$ increase. At the end of the burning the most abundant nuclides are $^{28}\mathrm{Si}$, $^{32}\mathrm{S}$, $^{38}\mathrm{Ar}$, $^{34}\mathrm{S}$, $^{36}\mathrm{Ar}$ and $^{40}\mathrm{Ca}$. During the O-burning, the neutron excess increases by a factor five ($\eta \approx 0.007$), making the composition of the core matter dramatically different from a solar system abundance distribution.

2.3.6 Si-burning

With the conclusion of the core oxygen burning and the depletion of $^{16}\mathrm{O}$, the composition is dominated by $^{28}\mathrm{Si}$ and $^{32}\mathrm{S}$. The core starts again to contract and the temperature rises. The fusion reactions $^{28}\mathrm{Si} + {}^{28}\mathrm{Si}$ and $^{32}\mathrm{S} + {}^{32}\mathrm{S}$ are unlikely to occur, because the Coulomb barriers of these nuclei are too high even at the extreme temperatures achieved at the end of massive stars evolution. Therefore, the nucleosynthesis proceeds via photodisintegration reactions of less tightly bound species and the subsequent capture of the liberated light particles to produce heavier and more tightly bound nuclei. This process takes the form of a complex network of forward and reverse reactions that eventually reach equilibrium. With increasing temperature and progressing time several pairs of nuclides link together to form quasi-equilibrium clusters. This photodisintegration rearrangement process is the silicon burning (Si-burning). It resembles the situation encountered with neon burning, but on a larger scale, gradually transforming $^{28}\mathrm{Si}$, $^{32}\mathrm{S}$ and other species in the $A = 24 - 46$ mass range in the iron peak nuclides, providing at the same time a new source of energy for the star. The temperatures characterizing this process are on the range $T = 2.8 - 4.1\,GK$. Assuming the core composition is exclusively made of $^{28}\mathrm{Si}$ and $^{32}\mathrm{S}$, the proton, neutron and α separation energies for these two nuclei are $S_p = 11.60\,MeV$,$S_n = 17.20\,MeV$,$S_\alpha = 9.98\,MeV$ and $S_p = 8.90\,MeV$,$S_n = 15.00\,MeV$,$S_\alpha = 6.95\,MeV$ respectively. As $^{32}\mathrm{S}$ is the more fragile nucleus, it is destroyed first in the $^{32}\mathrm{S}(\gamma,\alpha)^{28}\mathrm{Si}$ and $^{32}\mathrm{S}(\gamma,\mathrm{p})^{31}\mathrm{P}$ reactions that are followed by many sequences, such as $^{31}\mathrm{P}(\gamma,\mathrm{p})^{30}\mathrm{Si}(\gamma,\mathrm{n})\,^{29}\mathrm{Si}(\gamma,\mathrm{n})\,^{28}\mathrm{Si}$, converting $^{32}\mathrm{S}$ to $^{28}\mathrm{Si}$. Then the temperatures become high enough to photodisintegrate

effectively also ^{28}Si, starting a complex nucleosynthesis that progressively transforms Si and other intermediate mass species into iron peak nuclides. The nuclear network calculations were performed by Iliadis [2015] at $T = 3.6\,GK$ and $\rho = 3 \times 10^7\,g/cm^3$. These values are similar to those obtained by Chieffi et al. [1998] and Woosley et al. [2002] for a $25\,M_\odot$ stellar model with initial solar composition. These models also predict significant abundance variations at $T > 2.2\,GK$ just in between the end of oxygen burning and the beginning of silicon burning, with a decrease of ^{32}S and an increase in ^{30}Si and ^{34}S that implies also a growth of the neutron excess parameter η. The initial value of this parameter affects the silicon burning nucleosynthesis. The initial abundances for the network calculation where chosen as $X_{^{28}\mathrm{Si}} = 0.70$ and $X_{^{30}\mathrm{Si}} = 0.30$, resulting in an initial neutron excess parameter of $\eta = 0.02$. The abundance evolution show a downward flow from ^{24}Mg to ^{4}He produced by the photodisintegration of the initial fuel consisting only of ^{28}Si and ^{30}Si. Then the recapture of the α, p and n particles gives rise to an upward flow through numerous secondary reactions. Most of the activity takes place in the $A = 25 - 40$ and the $A = 46 - 64$ mass range, representing quasi-equilibrium clusters. The abundances of nuclides with $A < 40$ gradually decrease, while the iron peak species abundances increase. After just $t = 4000\,s$ the silicon fuel is exhausted in the core, which now is composed mostly ($\approx$) by ^{56}Fe, ^{52}Cr, ^{54}Fe, ^{55}Fe and ^{53}Mn. Initially, the neutron excess remains approximately constant, but then increases consistently due to the electron captures happening at the iron peak such as $^{23}\mathrm{Mn}(\mathrm{e}^-, \nu)^{53}\mathrm{Cr}$. The final neutron excess parameter reaches a value $\eta = 0.067$. It is interesting to notice that if the initial abundances are placed in argon and sulfur instead of silicon isotopes, the final abundances are the same as long as η remains unchanged. However, even a small change in the neutron excess parameter can produce a strong deviation in the final abundance distribution of the iron peak species, that is in any case very different from a solar system distribution due to the extremely large value of η. The products of silicon burning are then completely reprocessed by the subsequent phases of explosive burning and partially ejected in the interstellar medium. The core collapse and supernova explosion depend critically on the core composition and hence by the neutron excess produced by the silicon burning. The computed evolution for $T = 3.6\,GK$ and $\rho = 3 \times 10^7\,g\,cm^{-3}$ shows that the rate of consumption of ^{28}Si is three orders of magnitude smaller than its photodisintegration rate. This is due to the ^{28}Si photodisintegration flow being almost identical to the ^{24}Mg upward flow, slowing down the conversion of ^{28}Si. The energy generation rate during silicon burning cannot be described precisely, due to the complexity of nuclear transformations during this phase. For sure it depends on the temperature and density conditions, but also on the neutron excess. An order of magnitude estimate can be obtained assuming a very small initial neutron excess $\eta \approx 0$, that weak interactions are negligible and that for each two ^{28}Si nuclei destroyed a ^{56}Ni nucleus is produced. The calculation at $T = 3.6\,GK$ gives an energy generation rate that follows the relation $\epsilon_{Si}(T) \propto T^{47}$. Since so many nuclides achieve quasi-equilibrium, the thermonuclear rates of most reactions are not important for the nucleosynthesis and energy production dur-

ing silicon burning. More important are the binding energies (or Q-values), the nuclear masses, spins and weak interaction rates. The first two quantities are well known close to stability. However, the thermonuclear rates are needed to study those reactions that are not in quasi-equilibrium for a significant amount of time during Si-burning.

2.3.7 Nuclear statistical equilibrium

When also ^{28}Si disappears at the end of silicon burning, the temperature in the core raises consistently. At some point even the previously nonequilibrated reactions involving $A < 24$ species reach equilibrium, with the last being the $3\alpha \rightarrow {}^{12}$C reaction. At this point every nuclide in the network is in equilibrium via strong and electromagnetic interactions. The general picture is that of one large quasi-equilibrium group extending from p, n and α particles to the iron peak nuclei. This is the so called nuclear statistical equilibrium (NSE), that will be discussed in more detail in the next chapter. In nuclear statistical equilibrium the abundance of any nuclide can be determined by the repeated application of the Saha equation. The behaviour of this equation can be studied in the simplest case, with $\eta \approx 0$, assuming that weak interactions are negligible and that the ^{28}Si produced mainly ^{56}Ni. With the additional assumption that the stellar plasma consists entirely of ^{56}Ni and ^{4}He, one can study the conditions of temperature and density for which the mass fractions of these two nuclides are equal. Similarly, another boundary can be obtained for the case in which the composition is exclusively made of ^{4}He and nucleons in equal amounts. The result is shown in Fig. 2.1a. We see that, at lower temperatures, ^{56}Ni dominates the composition, at intermediate ones ^{4}He is the main constituent, and at higher temperatures matter is mostly made up of nucleons. Therefore, for a given value of density, with rising temperatures the composition shifts to lighter particles. The domain in which heavier nuclei dominate is located left of the solid line in Fig. 2.1a. In this region the dominant constituents depends on the value of the neutron excess parameter η or, equivalently, on electron fraction Y_e. If the plasma would consists of only one species, then η must be equal to the individual neutron excess $(N-Z)/A$ of this nuclide. It can be assumed that the maximum abundance for each nuclide is located near its individual neutron excess. This means that, in general, the most abundant nuclide in a composition of neutron excess η is the one with an individual neutron excess $(N-Z)/A \approx \eta$ and with the largest binding energy. The abundances of the dominant nuclides in a NSE composition at $T = 3.5\,GK$ and $\rho = 10^7\,g/cm^3$ versus η or Y_e are shown in Fig. 2.1c. For given values of temperature and density, the time needed to establish NSE can be calculated from the numerical expression

$$\tau_{NSE} = \rho^{0.2} e^{179.7/T_9 - 40.5}\, s \tag{2.19}$$

where ρ is in units of gram per cubic centimeter. So, this time depends strongly on temperature, as can be seen in Fig. 2.1b.For $T = 4\,GK$, it amounts to about 1 hour, but at $T = 6\,GK$ it reduces to just $\approx 10^{-3}\,s$: at higher temperatures

NSE can be achieved also in explosive events. The neutron excess at the end of silicon burning amounts to $\eta_f = 0.067$, but the extreme temperature and density reached in the core are accompanied by weak interactions that continuously change this parameter and the NSE composition adjusts accordingly. For example, in the last pre-supernova model of Chieffi et al. [1998], the core temperature and density are $T = 5.5\,GK$ and $\rho = 1.6 \times 10^9\,g/cm^3$ respectively with a neutron excess parameter $\eta = 0.13$, resulting in a composition dominated by ^{60}Fe, ^{64}Ni and ^{54}Cr. The internal structure of the star at this point of its evolution is characterized by the presence of many nested layers: those in which a particular burning is taking place and those constituted by the ashes of the overlying burning shell. The silicon burning continues in a shell that separates the silicon dominated layer, produced by the oxygen burning, from the iron core; the transformation of oxygen to silicon proceeds in a shell separating the oxygen and silicon layers and so on. The subsequent dramatic evolution depends on the physical conditions that develop in the iron core.

2.4 Core-collapse

Before the collapse, the temperature and density in the core amount to $T \approx 10\,GK$ and $\rho \approx 10^{10}\,g/cm^3$ respectively, conditions under which the nuclear statistical equilibrium is well established. The silicon burning shell continues to provide the iron peak nuclides that increase the mass of the core, which is at this point completely degenerate and supported by electron degeneracy pressure. When the mass of the core reaches the Chandrasekhar mass, even this pressure is no more sufficient to maintain the hydrostatic equilibrium and it becomes unstable to gravitational collapse. This limit depends on the core's composition and amounts to $M_{Ch} = 5.86\,Y_e^2\,M_\odot$ (Iliadis [2015]), where Y_e is the electron fraction. Its value is typically close to $M \approx 1.4\,M_\odot$, but depends sensitively on Y_e. Therefore, the collapse and infall dynamics are strongly determined by the electron fraction Y_e and also by the entropy per baryon s, which is related to the photon-to-baryon ratio ϕ by

$$s \sim 10\phi \sim \frac{T^3}{\rho} \tag{2.20}$$

Therefore, s depends on the number of photons, implying that the effect of s on the NSE composition is either to favor heavier nuclides if it's small or the photodisintegration of heavier nuclei into free nucleons if it's large. The early stages of core collapse are characterized by two effects that accelerates it. First, the density of electron increases and so the electron capture (e^-, ν_e) into nuclei, reducing the pressure exerted by electron degeneracy. Second, the high temperatures make the radiation sufficiently energetic to photodisintegrate iron peak nuclides into lighter species, to the detriment of the internal energy that could have provided pressure. These factors destabilize the core, that subsequently collapses, going from a several thousands kilometers sphere to a proto-neutron star of about ten kilometers radius within a fraction of a second.

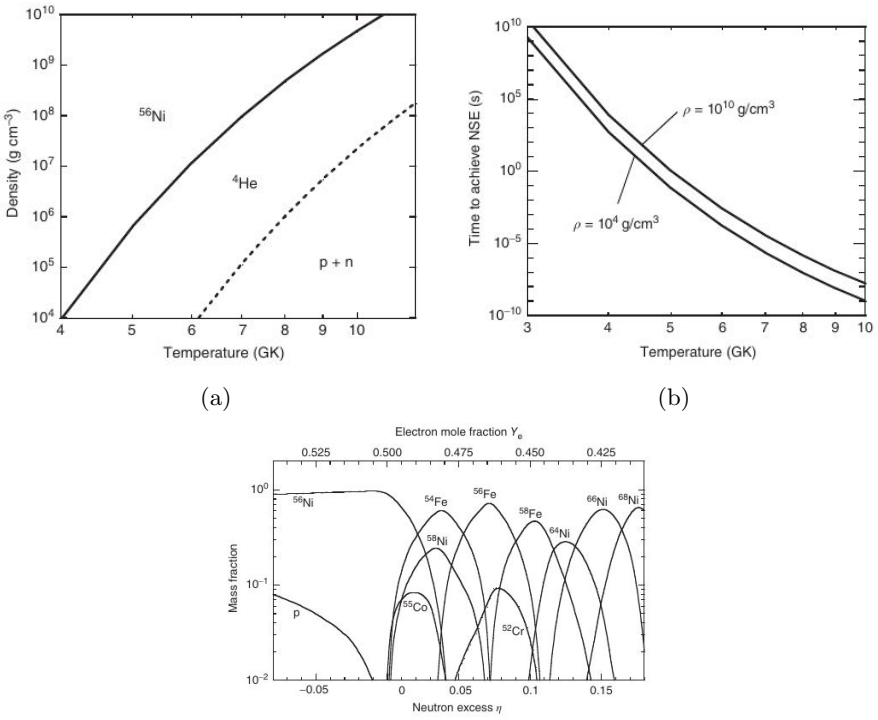

Figure 2.1: Panel (a): temperature-density conditions in a plasma at NSE with neutron excess parameter $\eta \approx 0$. The lines define regions of the dominant nuclear constituents. Panel (b): approximate time to reach NSE versus temperature. The lines are computed for two different densities ($\rho = 10^4\,\mathrm{g\,cm^{-3}}$ and $\rho = 10^{10}\,\mathrm{g\,cm^{-3}}$). Panel (c): abundances of the dominant species versus neutron excess parameter η or Y_e in a NSE composition at $T = 3.5\,\mathrm{GK}$ and $\rho = 10^7\,\mathrm{g\,cm^{-3}}$ [Images adapted from Iliadis, 2015]

.

Chapter 3

NSE: nuclear statistical equilibrium

At the end of Si-burning, temperature T and density ρ in the iron core are very high with $0.1 < T_9 < 5$ ($T_9 = T/10^9\,\mathrm{K}$) and $10^5 < \rho/\mathrm{g\,cm^{-3}} < 10^{10}$. At high temperatures, typically $T > 4$ GK ≈ 0.3 MeV the photon energy in an astrophysical plasma is high enough to dissociate nuclei into nucleons. On the other hand for densities in the range $10^6 < \rho/\mathrm{g\,cm^{-3}} < 10^{13}$ nuclear reactions are fast, leading to the formation of nuclei. In this situation strong and electromagnetic interactions are at equilibrium, the so called nuclear statistical equilibrium (NSE) and the composition of the core is given by nuclear Saha equation as function of T, ρ, the electron fraction Y_e, binding energy and nuclear partition function of each nucleus. The evolution of the star at this point is dramatically affected by these NSE conditions as the Chandrasekhar mass scales as $M_{Ch} \propto Y_e^2$.

Electron Fraction (Y_e) : In nuclear physics, the electron fraction refers to the number of electrons per baryon, typically denoted in environments where nuclear reactions occur under extreme temperature and pressure conditions. Mathematically, it is defined as:

$$Y_e = \frac{n_e}{n_b},$$

where n_e represents the number density of electrons and n_b represents the number density of baryons (neutrons and protons).

Scientific Context for Massive Stars : In the evolution of massive stars, the electron fraction plays a crucial role in determining the fate of the star during its final stages. During core collapse supernovae, for instance, the electron fraction influences the composition and dynamics of the collapsing core, affecting the details of the supernova explosion and the resulting compact remnant,

such as a neutron star or a black hole. Moreover, in scenarios involving the mergers of neutron stars, the electron fraction governs the properties of the ejected material and the formation of heavy elements through r-process nucleosynthesis. In the cores of massive stars, where temperatures and pressures are extreme, weak interactions, such as beta decay and electron capture, play a crucial role in determining the electron fraction. During stellar evolution, as the core contracts and temperature rises, electrons become increasingly energetic, promoting reactions such as electron capture by protons ($p + e^- \rightarrow n + \nu_e$) and beta decay ($n \rightarrow p + e^- + \bar{\nu}_e$). These processes can alter the electron fraction, influencing the balance between electron degeneracy pressure and gravitational collapse. Understanding weak interactions in massive stars is essential for predicting their evolution and eventual fate, including supernova explosions and the formation of compact remnants such as neutron stars.

3.1 NSE review and theory

Key Aspects of NSE:

1. **Thermal Equilibrium**: NSE assumes that the stellar material is in thermal equilibrium, meaning that the temperature throughout the stellar core is uniform.

2. **Equilibrium between Fusion and Photodisintegration**: In NSE, the rates of nuclear fusion reactions converting lighter elements into heavier ones are balanced by the rates of photodisintegration reactions breaking heavier elements into lighter ones. This equilibrium leads to stable nuclear compositions.

3. **Charge Neutrality**: NSE maintains charge neutrality, ensuring that the total positive and negative charges are balanced. This balance is crucial for the stability of the stellar core.

4. **Energy Balance**: NSE achieves energy balance through nuclear reactions, where the energy released from fusion processes balances the energy absorbed or emitted in photodisintegration reactions.

There are some important equations that must be considered in the calculation of NSE abundances. When NSE is reached the production and destruction of nuclei occur at the same rate and the chemical potential of nuclei and nucleons have to satisfy

$$\mu_{(Z,A)} = Z\mu_p + (A - Z)\mu_n \tag{3.1}$$

where the chemical potentials include the total mass

$$\mu_i = m_i c^2 + kT\eta_i + \mu_c \tag{3.2}$$

with η_i the degeneracy parameter, k the Boltzmann constant, T the temperature and μ_c the Coulomb contribution to the chemical potential. The electron

chemical potential is given by $\mu_e = m_e c^2 + \eta_e$. The abundance of the i isotope is $Y_i = n_i/n$ with n_i its number density and n the total baryon number density. Assuming Maxwell-Boltzmann (M-B) statistics, n_i is linked to the degeneracy parameter η_i by

$$n_i = \frac{G_i(T)e^{\eta_i}}{\Lambda_i^3} \tag{3.3}$$

with the partition function $G_i(T) = \sum(2J_k + 1)e^{-E_k/kT}$ with values calculated by Rauscher [2003] and the thermal wavelength $\Lambda_i = \sqrt{2\pi\hbar^2/m_i kT}$. At the considered densities also protons follow the M-B statistics, but neutrons become degenerate for $\rho \gtrsim 10^{11} g/cm^3$ (depending on T) so we use the Fermi-Dirac (F-D) distribution for both protons and neutrons

$$n_i = \frac{8\pi\sqrt{2}}{h^3} m_i^3 c^3 \beta_i^{3/2} [\mathcal{F}_{1/2}(\eta_i, \beta_i) + \beta_i \mathcal{F}_{3/2}(\eta_i, \beta_i)] \tag{3.4}$$

where $\beta = kT/mc^2$ is the relativistic parameter, which in the range of T considered is very close to 0 and $\mathcal{F}_k$ are Fermi functions

$$\mathcal{F}_k(\eta, \beta) = \int_0^\infty \frac{x^k (1 + \frac{1}{2}\beta x)^{1/2} dx}{e^{-\eta + x} + 1} \tag{3.5}$$

The electron mole number is defined as $Y_e = n_e/n$ where $n_e = n_{e^-} - n_{e^+}$ and the electron and positron number densities, n_{e^-} and n_{e^+} respectively, are related to their respective chemical potential by eq 3.4 with the condition $\mu_e = \mu_{e^-} = \mu_{e^+}$. Combining equations 3.1 and 3.3 we get the abundance Y of the nucleus with Z and A:

$$Y(Z, A) = \frac{G_{(Z,A)}}{\rho/m_u} \left(\frac{kTAm_u}{2\pi\hbar^2} \right)^{3/2} e^{(A-Z)\eta_n + Z\eta_p} e^{B/kT} e^{Z\mu_{c,p} - \mu_{c,(Z,A)}} \tag{3.6}$$

Here ρ is the baryon density, m_u the atomic mass unit, $B = Zm_p c^2 + (A - Z)m_n c^2 - m_{(Z,A)c^2}$ is the binding energy (from Audi et al. [2003] with theoretical values from Möller et al. [1995]). η_n and η_p are the degeneracy parameters, determined by charge neutrality and mass conservation

$$\sum Z_i Y_i = Y_e \tag{3.7a}$$

$$\sum A_i Y_i \tag{3.7b}$$

With equations 3.6, 3.7a and 3.7b we can get η_n, η_p and $Y(Z, A)$ for given T, ρ and Y_e.

3.1.1 Thermal weak and dynamical beta-equilibrium

To determine Y_e usually we must consider weak processes that are much slower than the strong and electromagnetic ones responsible for maintaining the NSE. However, if the system spends enough time at a given T and ρ, also these weak

reactions can reach equilibrium. When the neutrinos produced by them cannot leave the system the so called thermal weak equilibrium is reached. In this state neutrinos have a F-D spectrum with temperature T and the chemical potentials are $\mu_\nu = -\mu_{\bar{\nu}}$. When thermal weak equilibrium is reached the composition remains constant unless T or ρ changes. This means also entropy is conserved so $TdS = \sum_i \mu_i dY_i = 0$ and

$$\begin{aligned} \mu_\nu \dot{Y}_\nu + \mu_e \dot{Y}_e + \sum_i \mu_i \dot{Y}_i = \\ (\mu_e - \mu_\nu)\dot{Y}_e + (\mu_p - \mu_n)\sum_i Z_i \dot{Y}_i + \mu_n \sum_i A_i \dot{Y}_i = 0 \end{aligned} \tag{3.8}$$

with the right hand side coming from NSE assumption and the lepton number conservation condition $\dot{Y}_\nu = -\dot{Y}_e$. Using equations 3.7a and 3.7b the eq 3.8 reduces to

$$(\mu_e + \mu_p - \mu\nu - \mu_n)\dot{Y}_e = 0 \tag{3.9}$$

thus the value of Y_e for which equilibrium is attained is given by the condition

$$(\mu_e + \mu_p = \mu_\nu + \mu_n) \tag{3.10}$$

An alternative is given by equation

$$\begin{aligned} \dot{Y}_e = -\sum (\lambda^i_{ec} + \lambda^i_{\beta_+} + \lambda_{\bar{\nu}_e} + \lambda_{in\beta^-})Y_i + \\ + \sum_i (\lambda^i_{pc} + \lambda^i_{\beta^-} + \lambda^i_{\nu_e} + \lambda^i_{in\beta^+})Y_i = 0. \end{aligned} \tag{3.11}$$

Equation 3.11 requires knowledge of weak interaction rates of electron capture (ec), positron emission (β^+), antineutrino absorption ($\bar{\nu}_e$), inverse electron emission $in\beta^-$, neutrino absorption (ν_e) and inverse positron emission $in\beta^+$ for a large ensemble of nuclei. This makes equation 3.10 advantageous as it depends only on bulk nuclear properties of matter as partition functions and binding energies, but it can be applied only at very high densities as below $\sim 10^{11}\,\mathrm{g\,cm^{-3}}$ neutrinos escape and we can't define a neutrino chemical potential. In these cases a dynamical beta equilibrium can still be achieved with a Y_e equilibrium value given by the equation

$$\dot{Y}_e = -\sum_i (\lambda_{ec^i} + \lambda^i_{\beta^+})Y_i + \sum_i (\lambda^i_{pc} + \lambda^i_{\beta^-})Y_i = 0 \tag{3.12}$$

which is equation 3.11 after the suppression of neutrino absorption rates. An approximate solution for this equation can be provided by inserting $\mu_\nu = 0$ in the equation 3.10, which means that thermal weak equilibrium reduces to dynamical beta-equilibrium and the neutrino density is only T dependent, that is

$$n_\nu = n_{\bar{\nu}} = \frac{1}{2\pi^2\hbar^3}\int_0^\infty \frac{p^2}{1+\exp(pc/kT)}dp = 7.61\times 10^{27}\left(\frac{\mathrm{T}}{\mathrm{GK}}\right)^3 \mathrm{cm}^{-3} \tag{3.13}$$

with p being the neutrino momentum and pc its energy. The equation and approximation to use depend on the environment considered. At low temperatures the neutrino densities are negligibly small so the condition $\mu_\nu = 0$ reduces to $n_\nu = 0$. This is the condition of cold neutron stars where eq 3.10 is commonly used to determine the composition. At higher temperatures the equations of thermal weak equilibrium 3.10 and of dynamical beta-equilibrium 3.12 predict different values of Y_e: the former is no more a good approximation and the later one must be solved with a full set of weak interaction rates, that is a very challenging task. Anyway, to calculate the equilibrium Y_e at a given temperature and density, only a simple description of these rates is necessary as we are not interested in the full evolution towards equilibrium.

3.2 NSE calculation

The equations of NSE 3.6, 3.7a and 3.7b can be solved under the constraint of thermal weak equilibrium given by eq.3.10 with the assumption $\mu_\nu = 0$ for temperatures in the range $5 < T < 150\,\mathrm{GK}$ and $10^6 < \rho < 10^{12}\,\mathrm{g\,cm^{-3}}$. Assuming dynamic beta-equilibrium equation 3.12 the results are similar. This full solutions for the equlibrium electron fraction has been obtained by Arcones et al 2010. In the same paper the authors suggest some useful approximations that can give similar results to the full equations. T high temperatures ($T \gtrsim 15\,GK$) it can be assumed that only nucleons are present because all nuclei are dissociated, so $Y_e = Y_p$ and $Y_n = 1 - Y_e$. For low densities ($\rho \lesssim 10^8\,\mathrm{g\,cm^{-3}}$) the matter is mostly composed by non-degenerate neutrons, protons and electrons. This implies $\mu_e = 0$ and $\mu_n \approx \mu_p$ that together with eq 3.3 give

$$Y_e = \frac{1}{1 + e^{-\Delta/kT}} \tag{3.14}$$

where $\Delta = m_n - m_p = 1.293\,MeV$. At these conditions, if T becomes smaller than Δ, Y_e can reach high values. For higher densities this approximation is not valid anymore due to electron degeneracy. More precisely, this happens when

$$\rho \geq 1.132 \times 10^7 \frac{(kT)^{3/2}}{Y_e}(0.6773 + 2.256kT) \tag{3.15}$$

Above this limit the number density is approximately

$$n_e = 8\pi \left(\frac{kT}{hc}\right)^3 \frac{1}{3}\eta_e^3 \tag{3.16}$$

so we can get directly η_e from this equation and plug it in the equation 3.6 to estimate Y_e. If we assume that the nucleons follow a M-B distribution (eq 3.3), their chemical potentials are

$$\mu_{n(p)} = m_{n(p)}c^2 + kT \ln\left(\frac{n_{n(p)}\Lambda_{n(p)}^3}{G}\right) \tag{3.17}$$

Then, if we insert these in the beta-equilibrium equation $\mu_n = \mu_p + \mu_e$ we obtain

$$\Delta - m_e c^2 + kT \ln \left(\left(\frac{m_p}{m_n} \right)^{3/2} \frac{1 - Y_e}{Y_e} \right) - \left(\frac{3 Y_e \rho}{8\pi m_u} \right)^{1/3} \frac{hc}{kT} = 0 \tag{3.18}$$

which is a non-linear equation for the electron fraction that can be solved numerically using as guess value the Y_e given by 3.14. When the temperature is below $T \lesssim 15\, GK$ the presence of bound nuclei makes the situation more complex. Two domains can be defined: one in which heavy nuclei represent half of the total mass and one in which α particles represent half of the mass. These domains are identified in the $\rho - T$ plane by

$$\log \rho = 11.62 + 1.5 \log T_9 - \frac{39.17}{T_9} \tag{3.19}$$

in the first case and for the second one by

$$\log \rho = 29.68 + 4.5 \log T_9 + \log \frac{X_\alpha}{X_p^2 X_n^2} - \frac{142.62}{T_9} \tag{3.20}$$

in which X_α, X_n and X_p are the alpha, neutron and proton mass fractions respectively, obtained by mass and charge conservation equations

$$1 = X_\alpha + X_p + X_n \tag{3.21a}$$

$$Y_e = \frac{1}{2} X_\alpha + X_p \tag{3.21b}$$

At low densities, between the lines given by equations 3.19 and 3.20 in the $\rho - T$ plane, there are mostly alpha particles, therefore $Y_e = 0.5$. At high density the nuclei become neutron rich. Here other simple approximations can be applied, but the detailed composition and electron fraction can be derived only by numerical solving the full NSE equations under the conditions of thermal weak or dynamical beta-equilibrium. The solutions for the two assumptions are shown respectively in Figs. 3.1 and 3.2.

In the literature there are different studies that tackle the importance of the electron fraction and its effects within the evolution of massive stars. Arcones et al. [2010] focuses on the impact of NSE-related assumptions, primarily those of weak thermal equilibrium and dynamical β equilibrium, over a very wide parameter space. As far as stellar evolution is concerned, they found an uncertainty on the electron fraction Y_e of the order of few points per cent (see for example Figs. 3.1 and 3.2). A recent study by Renzo et al. [2024], instead, focuses on the details of the nuclear reaction calculations employed in stellar evolution codes and their effect on the predicted electron fraction at the end of the evolution of a massive star. They indicate that the resulting uncertainty is of order $1 - 3\%$ (as shown in Fig. 3.3). The uncertainty on Y_e propagates directly into an uncertainty on the chemical abundances resulting from nuclear reactions, but, as a result, it can also have an impact on the structural properties of

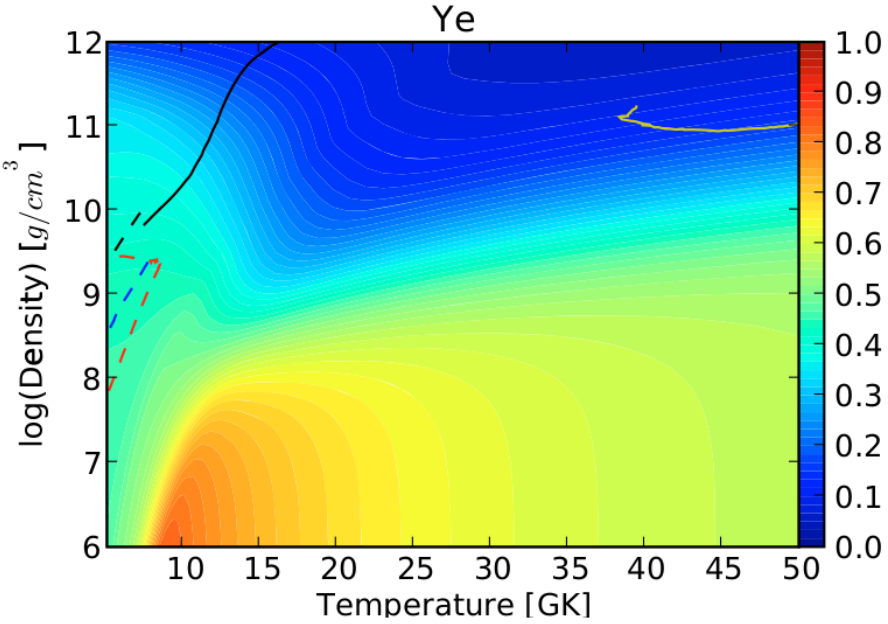

Figure 3.1: Electron fraction Y_e as a function of temperature and density with the assumption of thermal weak equilibrium from Arcones et al. [2010]

the innermost stellar layers. As a consequence, the uncertainty on the electron fraction affects the conditions for the explodability and final fate of the star. This topic has been approached, for instance, by O'Connor and Couch [2018], who focus on the impact of anisotropies in the Y_e distribution on the explosion mechanism. These authors performed detailed three-dimensional simulations to find a correlation between Y_e and the asymmetric neutrino heating mechanism (understood to power the supernova explosion) from a proto-neutron star. There are, however, fewer studies on the impact of Y_e during the phases before core-bounce. On top of this, there are many uncertenties on the collapse of the stellar core and the possible consequent explosion (see Janka [2012] and Janka [2024] for a review). Modern criteria for assessing the explodability of a massive star (O'Connor and Ott [2011], Ertl et al. [2016]) highlight the importance of the core compactness, i.e. its density distribution, that can be affected by the electron fraction under NSE conditions. In this work I probe the potential impact of Y_e and its uncertainty on the abundances and structure of the core of evolved massive stars.

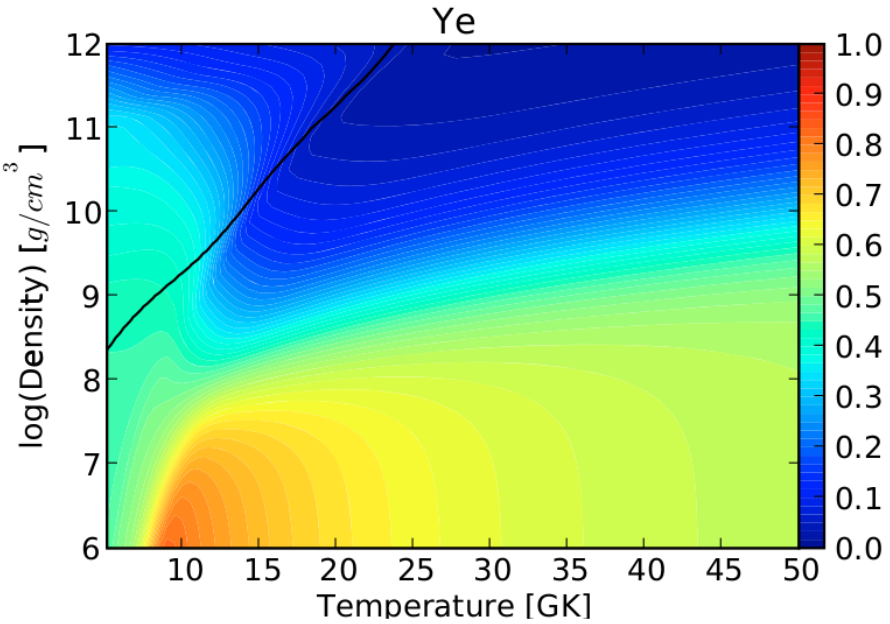

Figure 3.2: Electron fraction Y_e as a function of temperature and density with the assumption of dynamical-beta equilibrium from Arcones et al. [2010]

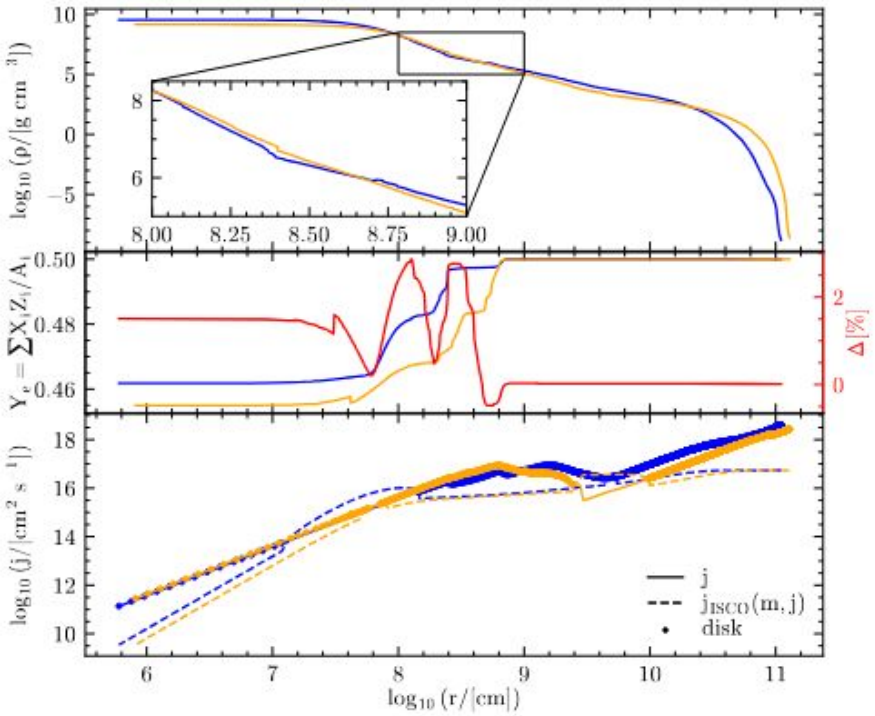

Figure 3.3: Comparison of $40M_{\odot}$ chemically homogeneous stellar models at the onset of core-collapse. The models differ only in the nuclear reaction network: `mesa_128` for the orange one and `approx21_plus_cr56` for the blue one. Top panel: density profile. Middle panel: Y_e profile and, in red, the relative variation of Y_e between the models (right vertical axis). Bottom panel: specific angular momentum j profile. Credits: Renzo et al. [2024]

Chapter 4

Methods

In this chapter I present the numerical methods adopted in the present work, that aims at studying the impact of the electron fraction during the late evolution of massive stars. In that situation, the composition of the stellar core depends on its physical conditions at the end of silicon burning, the most important of which are temperature T, density ρ and electron fraction Y_e. In order to obtain realistic combinations of these three quantities, I adopt `MESA` (version `r23.7.3`) (Modules for Experiments in Stellar Astrophysics), a modular stellar evolution code Paxton et al. [2011], Paxton et al. [2013], Paxton et al. [2015], Paxton et al. [2018], Paxton et al. [2019]. `MESA` includes a pre-assembled, general-purpose one-dimensional stellar evolution code called `star`. I used this code to calculate stellar evolutionary tracks for different initial masses, and to compare the features of the resulting models, with a particular focus on the central temperature, density, electron fraction and the abundances of some important species. Other important information can be retrieved with the code `public_nse` provided in Frank Timmes' web page ("COCOCUBED")COC. This tool is designed to calculate isotopic abundances at different values of T, ρ and Y_e, and is presented in Seitenzahl et al. [2008]. In the next sections I will address in more detail the description of each step.

4.1 Stellar evolution calculation

`MESA/star` (or simply `star`) is an open source software that approaches stellar physics, structure and evolution with modern numerical methods and updated physics, enabling it to evolve stellar models across challenging phases such as the advanced nuclear burnings, that have been a serious challenge in the past. `MESA` comes with microphysics modules that provide the physical properties of stellar matter:

1. The `rates` module contains more than 300 thermonuclear reaction rates for elements up to nickel and the weak reactions needed for hydrogen burning (e.g. positron emission and electron capture).

2. The `weaklib` module addresses lepton captures and $\beta-$decay rates for the high densities and temperatures encountered at the later stages of stellar evolution.

3. The `screen` module calculates electron screening factors for thermonuclear reactions in both the weak and strong regimes.

4. The `neu` module computes energy-loss rates and related quantities, due to neutrinos generated by plasmon decay, pair annihilation, bremsstrahlung, recombination and photo-neutrinos.

5. The nuclear reaction networks are implemented with the `net` module.

6. An alternate module, useful for large networks, is called `jina` and uses the JINA REACLIB database for thermonuclear reaction rates JIN. Since the 2019 MESA update Paxton et al. [2019], the `JINA REACLIB` library provides the default nuclear reaction rates. The nuclear partition functions use `JINA winvene_v2.0.dat` table and `JINA`. `masslib_library_5.data` provides the atomic masses.

`star` comes with a variety of test suites that represent a useful starting point for producing custom simulations of stellar evolution. The available suites differ by the adopted modules, configuration files ("inlist"), and input parameters, and provide examples for investigating different processes of stellar physics. To compute stellar tracks for this thesis I chose the massive star suite `20M_pre_ms_to_core_collapse`. As its name suggests, it evolves a $20M_{\odot}$ star from the main sequence to the core collapse phase. This test suite is divided into seven parts, each controlled by a different `inlist` file:

1. `inlist_make_late_pre_ms`, that creates a pre-main sequence model using the mass, metallicity, wind and rotation parameters contained in the file. `inlist_mass_Z_wind_rotation` and evolves it for 100 years.

2. The second part `inlist_to_zams` evolves the model to the zero age main sequence.

3. The third part, `inlist_to_end_core_he_burn`, takes the model to the core helium depletion.

4. The fourth part is controlled by the file `inlist_remove_envelope` that bridges the immediate post-core He-burning with subsequent phases, removing this stellar envelope (if some mass-loss prescription is enabled).

5. The fifth part, `inlist_to_end_core_c_burn`, the model is taken to core carbon depletion.

6. Part six evolves the model to $\log T = 9.60$ with `inlist_to_lgTmax`, corresponding approximately to silicon shell burning.

7. Finally, `inlist_to_cc` evolves the model until the final stages preceding core collapse.

The initial conditions of the simulation are set in the file `inlist_mass_Z_wind_rotation`, in particular the initial mass, metallicity, mass loss and rotation. In this case, I computed evolutionary tracks for initial masses 15, 20, 25, 30, 35, 40, 50, 60, and 75 $M_{\odot}$. All these values are well within the capabilities of the adopted code and suite, which were tested by their authors up to 80 $M_{\odot}$. I adopted solar metallicity and assumed zero mass-loss and no rotation. This rather strong assumption will be discussed in Ch. 6. An infall velocity $v_{\rm inf}$ of the iron core equal to $v_{\rm inf} = 10^7\,{\rm cm\,s^{-1}}$ was chosen as the stopping condition for the simulations. The output consists of a `history` file for each run (in this case, for each value of initial mass), containing the physical parameters of the stellar model at selected time-steps of the simulation, and a series of `profile` files with the physical conditions and composition across the star. More precisely, the `history.data` files contain, among others, the central values of temperature and density of the stellar models and also the effective temperature and luminosity during their lifetimes. The `history` files do not include detailed information about the abundances, so I extracted these values from the `profile` files, focusing in particular on the elements ^{28}Si, ^{54}Fe, ^{56}Fe and ^{56}Ni. This choice is motivated by the fact that these are expected to be among the most abundant isotopes during the Si-burning and later, when nuclear statistical equilibrium conditions are reached. I plotted the abundances of the four isotopes to produce Fig. 4.1, showing their abundance evolution for the $35M_{\odot}$ stellar model (the plots for the other stellar models are shown in Fig. A.1 in Appendix A). The evolution of the abundances of the four isotopes in the stellar cores is presented alongside the evolution of the core T, ρ and Y_e. From them it is possible to distinguish qualitatively some evolutionary burning stages of stellar evolution. The red line in Fig. 4.1, for example, shows the evolution of the ^{28}Si abundance. When it grows above zero, the production of ^{28}Si has initiated, so this represents the start of the core O burning. Its peak represents the end of O burning and the onset of Si burning. When this curve returns to zero, ^{28}Si has been depleted in the core and the burning has shifted to a shell. Therefore, using the data shown in these plots, I identified three key evolutionary moments for each isotope:

1. The time at which the abundance becomes non negligible (i.e. it starts being synthesized).

2. The time at which the abundance reaches the maximum.

3. The time at which it becomes depleted.

The abundances predicted by `star` at each of the three selected evolutionary times are also reported in table A.1 (in Appendix A).

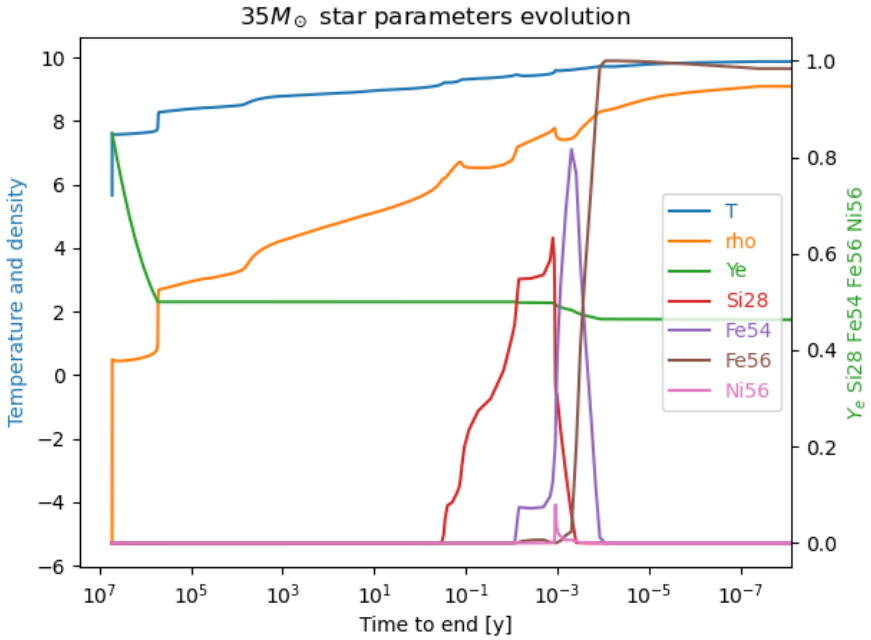

Figure 4.1: Abundances evolution for the $35M_\odot$ stellar track. x-axis: the time to the end of the simulation in years. Left y-axis: logarithmic temperature and density scale. Right y-axis: electron fraction Y_e and abundances scale.

4.2 Nuclear statistical equilibrium calculation

While `star` provides realistic physical conditions in stellar interiors, it is not trivial to use it for studying the direct impact of selected physical quantities. Indeed this would require editing or rewriting portions of the code, with possibly unexpected results. Instead, in order to explore the role of the electron fraction it is preferable to employ another code. For the present work, I adopted the `public_nse` tool available on Frank Timmes' web page "COCOCUBED" COC (`https://cococubed.com/code_pages/nse.shtml`) which puts a 47 isotope network into its NSE state. Compared to `MESA`, this code follows the formalism of Hartmann et al. [1985] for the chemical potentials and mass fractions, and sets the partition functions to their ground state value, whereas `MESA` makes use of JINA REACLIB that considers also excited states. The `public_nse` code takes the values of density, temperature, and electron fraction as input parameters and returns the abundances of free protons, free neutrons, and of the 47 isotopes of the network under NSE. These results can be used to study the behavior of the NSE abundances distributions at fixed values of two parameters as a function of the third one. In particular, I used the central values of electron fraction, temperature and density at the center of MESA stellar mod-

els corresponding to the three evolutionary times of ^{28}Si, ^{54}Fe, ^{56}Fe and ^{56}Ni described in the previous section. Since this work is focused on the role of the electron fraction, I studied how the abundances depend on this parameter by varying it around the value predicted by `star`, keeping ρ and T fixed. After computing NSE abundances with `public_nse`, I compared the results (that will be presented in the next chapter) with the predictions of `MESA`, as illustrated in Figs. 4.2 and 4.3. The evident discrepancies are most likely due to the resources optimization options adopted in the `MESA` calculations, whereas the predictions of `public_nse` are expected to be more realistic. I verified this expectation by cross-checking the results with the output of `pynucastro`, an open-source library for nuclear astrophysics with easy-to-use Python interfaces. Several tests performed with `pynucastro` show good agreement with `public_nse`, with marginal discrepancies that can be attributed to the simplifying assumptions made in the latter. It should be noted that, compared to `pynucastro`, `public_nse` is substantially more stable, lightweight and flexible, and hence more suited for this study. The disagreement with respect to MESA results is further addressed in Ch. 6.

4.3 Estimating the impact of Y_e on the mass of ^{56}Ni in the core

The present work aims at assessing the impact of uncertainties in the value of Y_e on calculations of stellar structure and evolution. There are different ways to do so, and given the exploratory nature of this thesis, I chose to probe possible effects on the chemical composition of the pre-supernova core in terms of the ^{56}Ni abundance, proceeding as follows:

1. For each stellar track I recovered the information on the temperature, density and electron fraction stratification from the last `profile` file of each `MESA` simulation. The MESA `profile` files contain a large number of parameters that can be ideally divided in two categories: global parameters that characterize the profile as a whole and local ones that refer to each mass shell. Among the former ones we have the mass M_c of the iron core. This quantity can be used to select the reference mass coordinate representing the border of the core.

2. I take the values of temperature T, density ρ and electron fraction Y_e for each shell inside the iron core. In all cases the temperature is large enough [$T \gtrsim 4\times10^9$ K, Arcones et al., 2010] for the assumption of NSE to be valid, expect possibly at the very edge of the core of the $15M_\odot$ star.

3. I used the core profiles of T, ρ and Y_e to compute the NSE abundances with `public_nse` across each core.

4. Given the ^{56}Ni mass fraction $X_{^{56}\mathrm{Ni},i}$ in the shell i with mass dm_i, I com-

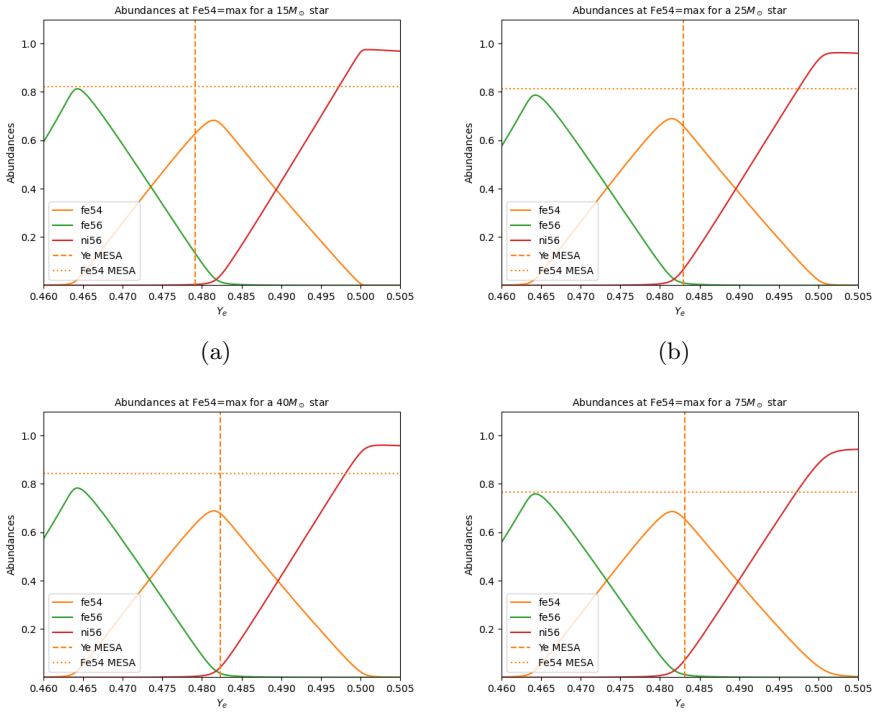

Figure 4.2: Abundances of ^{54}Fe, ^{56}Fe and ^{56}Ni calculated for the thermodynamic conditions corresponding to the peak abundance of ^{54}Fe, obtained with `public_nse`. The vertical dashed lines and horizontal dotted lines indicate, respectively, the value of electron fraction Y_e and the abundance of ^{54}Fe predicted by `MESA` (see A.1). Each panel corresponds to a different evolutionary track (initial masses: 15, 25, 40 and 75 $M_\odot$)

puted the amount of ^{56}Ni in solar masses by integrating through the core:

$$M_{^{56}\mathrm{Ni}} = \int_0^{M_c} X_{^{56}\mathrm{Ni}} dm = \sum_{i \leq M_c} X_{^{56}\mathrm{Ni},i} dm_i \,. \tag{4.1}$$

The quantity $M_{^{56}\mathrm{Ni}}$ represents the mass of ^{56}Ni contained in the core under the assumption of NSE, for the reference value of $Y_e = Y_e^0$ predicted by `MESA`. In order to assess the impact of the uncertainty on this parameter I repeated the above procedure after changing its value to $Y_e^k = Y_e + dY_e^k$, with $dY_e^k = kY_e^0$, taking several choices of k = [-0.03,-0.02,-0.01,0.01,0.02,0.03]. This allows me to study an uncertainty of the same order of magnitude as that found by Renzo et al. [2024].

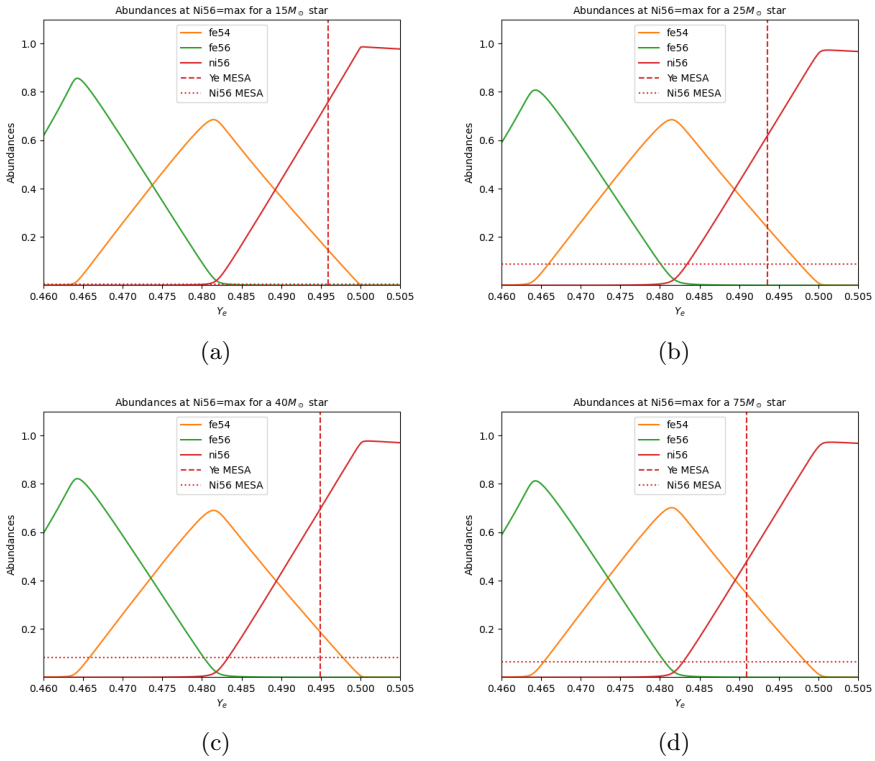

Figure 4.3: As in Fig. 4.2, but considering the peak abundance of ^{56}Ni.

For each track, I obtained this way six distinct estimates $M^k_{^{56}\mathrm{Ni}}$ of the ^{56}Ni mass in the core as a function of the assumed uncertainty of Y_e. These can be used to estimate the corresponding uncertainty on the ^{56}Ni mass itself:

$$\Delta M_{^{56}\mathrm{Ni}} = \frac{\max(M^k_{^{56}\mathrm{Ni}}) - \min(M^k_{^{56}\mathrm{Ni}})}{M^0_{^{56}\mathrm{Ni}}} \,. \tag{4.2}$$

The results are represented in Ch. 5.

4.4 Estimating the impact of Y_e on the total core mass

We can assume that a small uncertainty on Y_e does not change substantially the density stratification in the core, so I made the simplifying assumption of homology. The equations of continuity and momentum conservation become

(e.g. Kippenhahn, Weigert, and Weiss [2013]):

$$\frac{\rho_2}{\rho_1} = \frac{M_{\mathrm{c},2}}{M_{\mathrm{c},1}} \left(\frac{R_{\mathrm{c},2}}{R_{\mathrm{c},1}} \right)^{-3} , \tag{4.3}$$

$$\frac{P_2}{P_1} = \left(\frac{M_{\mathrm{c},2}}{M_{\mathrm{c},1}} \right)^{2} \left(\frac{R_{\mathrm{c},2}}{R_{\mathrm{c},1}} \right)^{-4} , \tag{4.4}$$

where the subscripts 1 and 2 refer to any two models to be compared (i.e. stellar cores with different assumptions on Y_e), ρ and P are the local density and pressure in homologous layers, and M_c and R_c are the mass and radius at homologous layers near the edge of the core. Combining Eq. 4.3 and Eq. 4.4 yields:

$$\frac{P_2}{P_1} = \left(\frac{M_{\mathrm{c},2}}{M_{\mathrm{c},1}} \right)^{2/3} \left(\frac{\rho_2}{\rho_1} \right)^{4/3} . \tag{4.5}$$

Given the conditions in the core, we can assume the equation of state to be that of an ideal classical gas with radiation:

$$P = P_\mathrm{gas} + P_\mathrm{rad} = \frac{\mathcal{R}}{\mu}\rho T + \frac{a}{3}T^4 = \left(\frac{3\mathcal{R}}{a} \right)^{1/3} \left(\frac{1-\beta}{\beta^4} \right)^{1/3} \left(\frac{\rho}{\mu} \right)^{4/3} , \tag{4.6}$$

where the meaning of the symbols is the usual one:

1. μ is the mean molecular weight of the gas.
2. $\beta = P_\mathrm{gas}/P$.
3. $\mathcal{R} = 8.314 \cdot 10^7 \,\mathrm{erg\,g^{-1}\,K^{-1}}$ is the ideal gas constant.
4. $a = 7.566 \cdot 10^{-15} \,\mathrm{erg\,cm^{-3}\,K^{-4}}$ is the radiation density constant, which is related to the Stefan-Boltzmann constant by $a = 4\sigma_\mathrm{SB}/c$.

By inserting Eq. 4.6 into Eq. 4.5, we obtain:

$$\frac{M_{\mathrm{c},2}}{M_{\mathrm{c},1}} = \left(\frac{f(\beta_2)}{f(\beta_1)} \right)^{3/2} \left(\frac{\mu_2}{\mu_1} \right)^{-2} , \tag{4.7}$$

having denoted $f(\beta) = (1-\beta)\beta^{-4}$. By similar arguments as before, we can assume the thermal stratification in the core to be only slightly altered by small changes in Y_e, so that $f(\beta)$ remains unchanged. Eq. 4.7 normally applies to chemically homogeneous conditions, so I needed to make a further simplification by taking a suitable average of μ over the core region:

$$\frac{1}{\langle\mu\rangle} = \frac{1}{M_\mathrm{c}} \int_0^{M_\mathrm{c}} \frac{1}{\mu(m)} \,\mathrm{d}m = \frac{1}{M_\mathrm{c}} \int_0^{M_\mathrm{c}} \left[\frac{1}{\mu_\mathrm{e}} + \frac{1}{\mu_\mathrm{i}} \right] \mathrm{d}m = \frac{1}{\langle\mu_\mathrm{e}\rangle} + \frac{1}{\langle\mu_\mathrm{i}\rangle} , \tag{4.8}$$

where μ_e is the mean molecular weight per free electron and μ_i is the mean molecular weight of the ions. I used these equations to investigate how the change in mean molecular weight affects the core mass, proceeding as follows:

1. I took the abundances of the 47 isotopes predicted by `public_nse` throughout the core.
2. I computed $\frac{1}{\mu} = \sum_i \frac{(Z_i+1)X_i}{A_i}$ for each shell, where Z_i, A_i and X_i are the atomic number, mass number and abundance of the ith isotope respectively.
3. I computed $\frac{1}{\langle\mu\rangle}$ with eq 4.8.
4. As $\frac{1}{\mu_e} = Y_e$, I computed $\frac{1}{\langle\mu_e\rangle}$ as $\langle Y_e\rangle$ across the core.
5. Having $\frac{1}{\langle\mu\rangle}$ and $\frac{1}{\langle\mu_e\rangle}$, I obtained $\frac{1}{\langle\mu_i\rangle}$ from eq 4.8.
6. I repeated the procedure for the other six sets of `nse_tool` output produced in the Y_e range described in the previous section.
7. I computed the ratio $\frac{\langle\mu^k_{Y_e}\rangle}{\langle\mu^0_{Y_e}\rangle}$, where k has the same meaning as in the previous section.
8. With the assumption that $f(\beta_2) = f(\beta_1)$, I computed $\frac{M^k_c}{M^0_c}$ using eq 4.7.

The results are presented in Ch. 5.

Chapter 5

Results

5.1 Stellar evolutionary tracks

I present in Fig. 5.1 the H-R diagram showing the evolution of the stellar models I computed with `MESA/star`. It should be noted that the plot is constructed using `history` files, that do not necessarily include information for all computational time-steps. The time resolution of these files is often limited for optimization purposes, resulting in some artificial features such as the spikes at $3.7 \lesssim \log(T_{\rm eff}/K) \lesssim 3.8$ appearing for a few tracks. This features don't affect the outcome of the computation, and in any case, this study is focused very final points of each track. Since the evolution of massive stars is heavily shaped by mass loss, the surface properties of the stellar tracks are not necessarily realistic, in contrast with the physics of the innermost layers that I am interested in studying (see Ch. 6). The conditions in the core are shown in Fig. 5.2, which displays the central temperature T_c and density ρ_c. As the core is described as an ideal gas with radiation, the slope of the tracks is close to 1/3 in this plane, as expected by a quasi-static homologous contraction of the core. Deviations from this behavior arise due to two effects [Kippenhahn et al., 2013]:

- at the transition between nuclear fuels the tracks deviate from homologous contraction once a new nuclear fuel is ignited and convection develops in the core;
- with progressively increasing density and temperature neutrino cooling becomes efficient, resulting in a shallower slope.

the former effect is more evident in Fig. 5.3, which shows an enlarged view on the tracks from the onset of O-burning and beyond. This figure also exemplifies the potential numerical difficulties inherent to the advanced burning stages of massive stars, highlighted by the artifacts around $\log \rho \approx 8$ for the $15 M_\odot$ track. I briefly considered again this aspect in Ch. 6. Crucially, Fig. 5.3 confirms that central temperatures since the beginning of Si-burning satisfy the NSE condition.

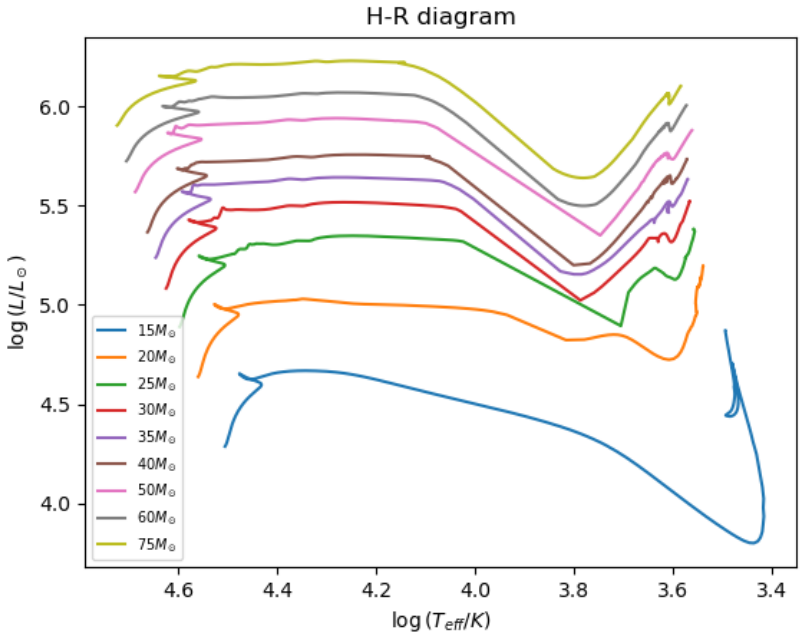

Figure 5.1: H-R diagram of the nine stellar models from ZAMS to core collapse

5.2 Impact of Y_e on ^{56}Ni mass in the core

In this section I present the results of the estimate of the ^{56}Ni abundance as described in Sec.4.3. As a first step it should be verified that the condition for NSE applies to the entire core for each track. To do so, I have examined the values of T and ρ at the center and the edge of the core, as well as in the shell located in between. These values are summarized in table 5.1. The requirement in terms of temperature is $T > 4 \times 10^9$ K, which is verified in all cases except near the border of the core for the lowest mass one among the tracks I computed.

This supports the correctness of the method adopted to compute the mass fraction and total mass of ^{56}Ni inside the core. The results of this procedure are displayed in Figs. 5.4 and 5.5 and are presented in table 5.2. The first column contains the masses of the stellar models, the second and third columns the temperature in the outermost shell of the core. In the fourth column there are the ^{56}Ni masses predicted by `public_nse` with the Y_e^0 value from `MESA`, while the other six columns contain the masses predicted with the Y_e^k values inside the uncertainty range. From the values in this table it's apparent that even small variation in Y_e can have a huge impact in the predicted ^{56}Ni mass. For a variation of $\pm 3\% Y_e$, the predicted masses differ of five orders of magnitude from one extreme to the other inside this range. This means that the resulting

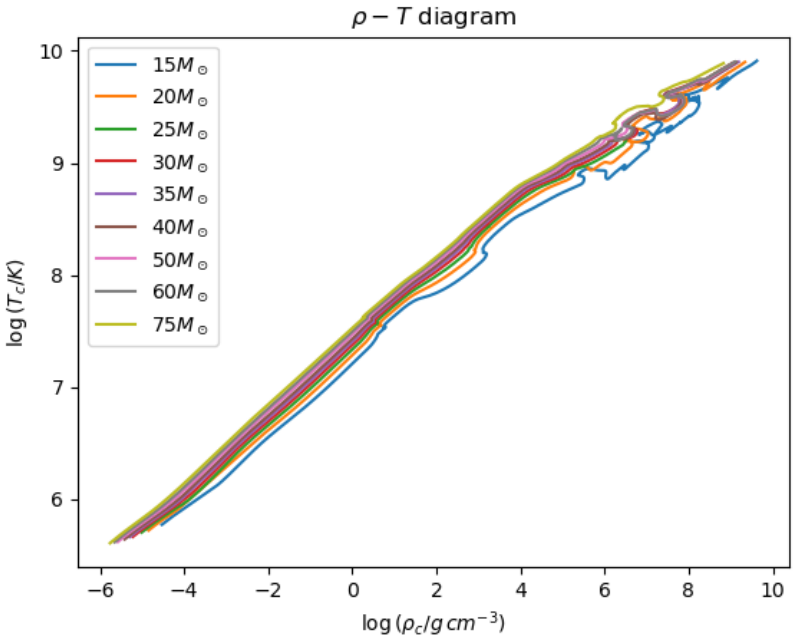

Figure 5.2: $\rho - T$ diagram for the nine stellar tracks. This plot shows how the central temperature T_c and density ρ_c of the stellar models computed with `MESA` evolve from ZAMS to core collapse.

uncertainties on NSE abundances can also be expected to be substantial. In particular, the change in the total mass of ^{56}Ni inside the core as a function of the assumed uncertainty dY_e is displayed in Fig. 5.6 and the corresponding relative uncertainty is summarized in table 5.3. In the third column I indicated the estimate over the range $\pm 3\% Y_e$ and in the fourth column over $\pm 1\% Y_e$. In both cases the values are extremely large, around ~ 20 for the largest range and ~ 5 for the more conservative one. To better understand these values, it should be kept in mind that the core masses predicted by `MESA` for the final models range between $1.5 M_\odot$ and $2.3 M_\odot$ and the corresponding mass of ^{56}Ni is of order $0.005 M_\odot$ to $0.1 M_\odot$. The high sensitivity of NSE reactions to Y_e is such that the amount of ^{56}Ni goes from a negligible level up to $15 - 20\%$ of the total core mass. A closer inspection of Figs. 5.4 and 5.5 show how the primary contribution to the total ^{56}Ni mass comes from the outer part of the core, this means that results for the $15 M_\odot$ star might be affected by the uncertain validity of NSE. However, this is not the case for the more massive tracks.

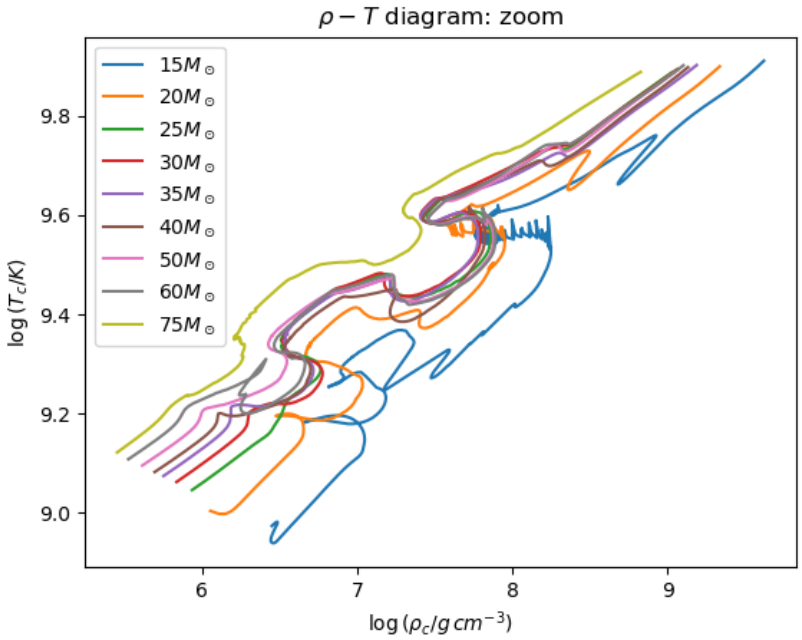

Figure 5.3: Zoom in of Fig. 5.2 focusing on the late evolutionary stages

$M\,[M_\odot]$	$T_b\,[GK]$	$T_m\,[GK]$	$T_c\,[GK]$	$\rho_b\,[10^7\,\mathrm{g\,cm^{-3}}]$	$\rho_m\,[10^8\,\mathrm{g\,cm^{-3}}]$	$\rho_c\,[10^9\,\mathrm{g\,cm^{-3}}]$	$Y_{e,b}$	$Y_{e,m}$	$Y_{e,c}$
15	3.68	5.82	8.15	1.72	3.13	4.18	0.48270	0.47160	0.46181
20	4.10	6.10	7.94	2.15	1.96	2.17	0.48207	0.47177	0.46284
25	4.52	5.94	7.83	1.41	0.41	1.16	0.48671	0.47910	0.46326
30	4.26	5.85	7.84	1.15	0.66	1.17	0.48425	0.47638	0.46313
35	4.43	6.02	7.99	1.69	0.73	1.54	0.48523	0.47540	0.46293
40	4.31	6.08	7.91	1.71	1.71	1.36	0.48340	0.47411	0.46315
50	4.36	5.86	7.70	1.42	0.63	1.10	0.48395	0.47665	0.46344
60	4.28	5.97	7.98	1.27	0.45	1.27	0.48407	0.47753	0.46295
75	4.37	5.79	7.74	0.82	0.46	0.67	0.48940	0.47820	0.46334

Table 5.1: T, ρ and Y_e at three positions in the stellar cores. The subscripts b, m and c stand for "border", the outermost shell, "middle", the shell equally distant from the center and the border of the core and "center", the innermost shell, respectively.

5.3 Impact of Y_e on the total core mass

The effective impact of these altered abundances is difficult to ascertain due to the complexity of the processes involved in the core collapse and explosion. Hence, it is interesting to probe the more global effect of Y_e on the core mass, which controls the evolution and the dynamics of the final stages of massive stars. The value of Y_e plays a role on the conditions that lead to the core's collapse. To quantify its impact we can study how the core's structure changes

$M\,[M_\odot]$	$log(T_b/K)$	$T_b\,[GK]$	$M^{0}_{^{56}\mathrm{Ni}}$	$M^{-0.01}_{^{56}\mathrm{Ni}}$	$M^{-0.02}_{^{56}\mathrm{Ni}}$	$M^{-0.03}_{^{56}\mathrm{Ni}}$	$M^{0.01}_{^{56}\mathrm{Ni}}$	$M^{0.02}_{^{56}\mathrm{Ni}}$	$M^{0.03}_{^{56}\mathrm{Ni}}$
15	9.57	3.68	5.09e-3	4.74e-4	7.33e-5	5.42e-6	3.60e-2	9.04e-2	1.69e-1
20	9.61	4.10	5.37e-3	6.46e-4	1.03e-4	7.22e-6	4.00e-2	1.00e-1	1.83e-1
25	9.65	4.52	1.44e-2	1.87e-3	3.26e-4	3.60e-5	6.05e-2	1.35e-1	2.29e-1
30	9.63	4.26	1.94e-2	1.90e-3	3.24e-4	3.63e-5	7.94e-2	1.70e-1	2.82e-1
35	9.65	4.43	7.14e-3	9.82e-4	1.61e-4	1.28e-5	4.11e-2	1.01e-1	1.81e-1
40	9.63	4.30	8.28e-3	1.08e-3	1.80e-4	1.39e-5	5.05e-2	1.22e-1	2.15e-1
50	9.64	4.36	1.39e-2	1.60e-3	2.75e-4	2.74e-5	6.62e-2	1.52e-1	2.62e-1
60	9.63	4.25	1.75e-2	1.69e-3	2.86e-4	3.22e-5	7.18e-2	1.53e-1	2.54e-1
75	9.64	4.37	1.02e-1	2.88e-2	2.52e-3	4.24e-4	1.97e-1	3.10e-1	4.27e-1

Table 5.2: Total ^{56}Ni mass in the core. T_b represents the temperature at the core's border or, equivalently, in the outermost shell. $M^{0}_{^{56}\mathrm{Ni}}$ indicates the total mass of ^{56}Ni contained in the core predicted with the Y_e value of MESA. The total masses predicted with other Y_e values are indicated as $M^{k}_{^{56}\mathrm{Ni}}$ in the other columns, where $k = -0.03, -0.02, -0.01, 0.01, 0.02, 0.03$.

$M\,[M_\odot]$	$log(T_b/K)$	$T_b\,[GK]$	$\Delta M^{\pm 0.03}_{^{56}\mathrm{Ni}}$	$\Delta M^{\pm 0.01}_{^{56}\mathrm{Ni}}$
15	9.57	3.68	33.26	6.98
20	9.61	4.10	34.05	7.34
25	9.65	4.52	15.96	4.08
30	9.63	4.26	14.55	4.00
35	9.65	4.43	25.40	5.62
40	9.63	4.31	25.91	5.96
50	9.64	4.36	18.83	4.65
60	9.63	4.28	14.52	4.01
75	9.64	4.37	4.19	1.66

Table 5.3: ^{56}Ni mass uncertainty for the nine stellar models. First column: initial masses of the models. Second and third columns: temperature at the border b of the core. Fourth and fifth columns: uncertainties on the ^{56}Ni mass arising from $\pm 3\%$ and $\pm 1\%$ variations on Y_e, respectively.

as function of Y_e and, in particular, its mass. The goal is to estimate how large is the error on the core mass prediction when there's an uncertainty on the Y_e value, following the procedure outlined in Sec.4.4. The results are exemplified in table 5.4 for the $15M_\odot$ model, which is representative of the overall behavior of all tracks, similar tables for other models are given in Appendix. Additionally, the results are shown in Figs. 5.7, 5.8, 5.10 and 5.9. In the left plot of Fig. 5.7, the mass-averaged mean molecular weight is plotted against dY_e. As Y_e drops, $\langle\mu\rangle$ increases covering changes of about $\pm 3\%$ over the explored range of Y_e uncertainty, as shown in the right panel of Fig. 5.7. The latter displays the ratios $\langle\mu^k\rangle/\langle\mu^0\rangle$ against dY_e, where $\langle\mu^0\rangle$ is the value of $\langle\mu\rangle$ computed with the reference value of Y_e provided by `star` and $\langle\mu^k\rangle$ are those computed at $Y_e + kY_e$. To better understand the behavior $\langle\mu^k\rangle$, in Fig. 5.8 I distinguish between the contributions from the mass-averaged mean molecular weight per free electron

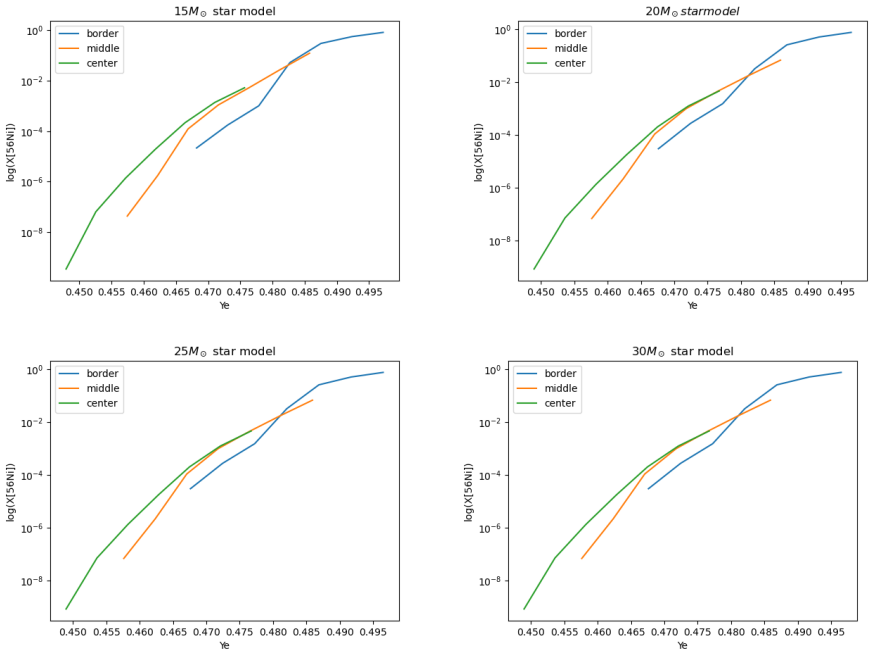

Figure 5.4: ^{56}Ni abundance as function of Y_e at the centre c, middle m and border b positions of the iron core for the $15M_\odot$, $20M_\odot$, $25M_\odot$ and $30M_\odot$.

($\langle\mu_e^k\rangle$) and the mass-averaged mean molecular weight per ion ($\langle\mu_i^k\rangle$). It is clear that the former dominates the overall behavior of $\langle\mu^k\rangle$, as it is much smaller (≈ 2) than $\langle\mu_i^k\rangle$ ($\gtrsim 30$). However, the dependence of these two quantities on Y_e arises from different effects. Increasing Y_e implies a higher number of lighter particles (i.e. e^-), but affects to a negligible level the mass of a parcel of gas, which is shared by a larger number of free particles, hence $\langle\mu_e^k\rangle$ decreases. At the same time, increasing Y_e alters the relative number of n compared to p, favoring the latter, altering the reaction equilibrium. So, different types of isotopes, with different mass numbers, are preferred when Y_e is varied, which is reflected in the changing value of $\langle\mu_i^k\rangle$, as can be seen in Fig. 5.8b. While $\langle\mu_e^k\rangle$ displays essentially the same behavior as a function dY_e for all the stellar models, $\langle\mu_i^k\rangle$ shows a slightly different functional form. As discussed in Sec.4.4, under suitable assumptions, one can use the value of $\langle\mu\rangle$ to obtain an approximate estimate of change of core mass resulting from variations on Y_e, as can be appreciated from Figs. 5.9 and 5.10. What can be seen is that for a given fractional variation of Y_e one obtains a twice as large relative change in M_c. However, as expected from the role of $\langle\mu_i^k\rangle$ the effect is different for distinct initial masses, with the heaviest stellar models suffering on average the smallest changes.

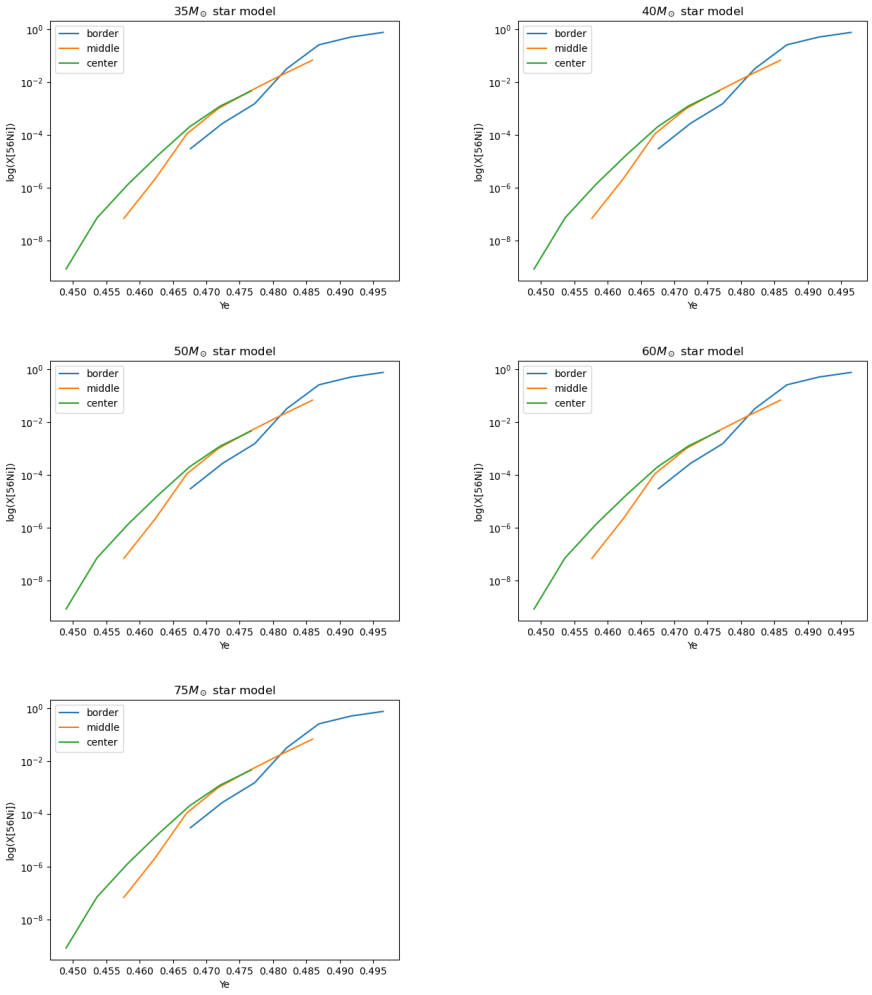

Figure 5.5: ^{56}Ni abundance as function of Y_e at the centre c, middle m and border b positions of the iron core for the $35M_\odot$, $40M_\odot$, $50M_\odot$, $60M_\odot$ and $75M_\odot$ stellar models.

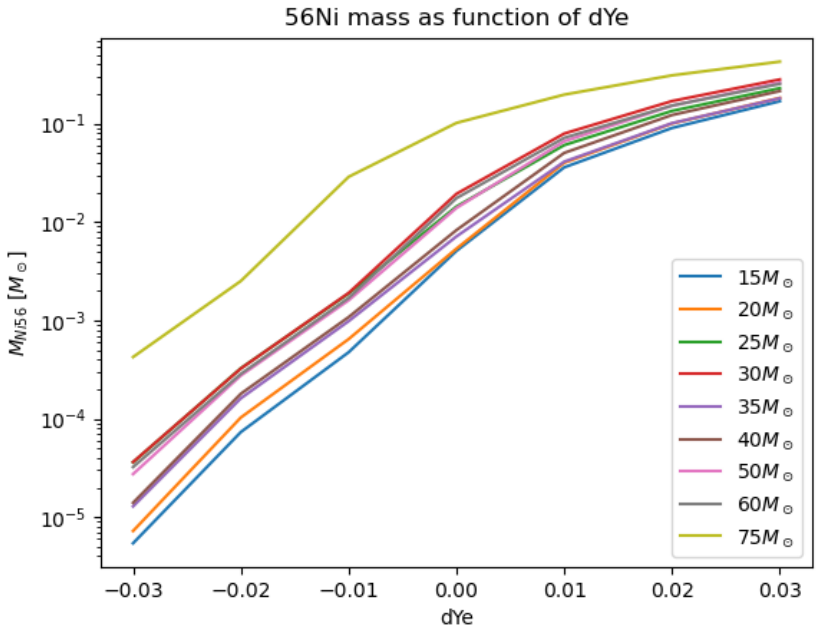

Figure 5.6: Total mass of ^{56}Ni in the iron core as function of Y_e variation for all stellar models computed in this work.

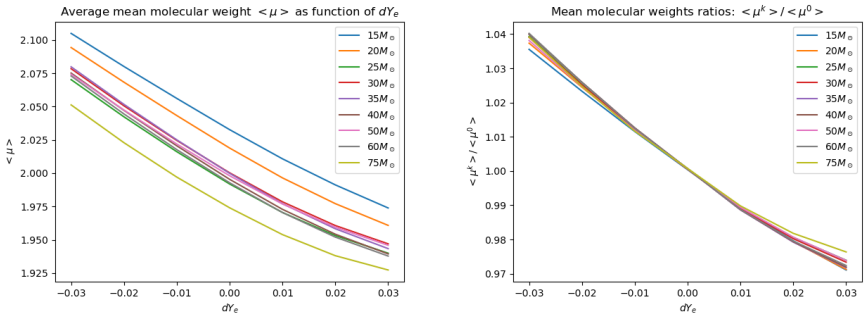

Figure 5.7: Average mean molecular weight $\langle\mu\rangle$ (left) and $\langle\mu^k\rangle/\langle\mu^0\rangle$ ratios (right) as function of dY_e, where $\langle\mu^0\rangle$ is the average mean molecular weight computed with the Y_e^0 value provided by `MESA` and $\langle\mu^k\rangle$ is the average mean molecular weight computed with $Y_e^0 + kY_e^0$.

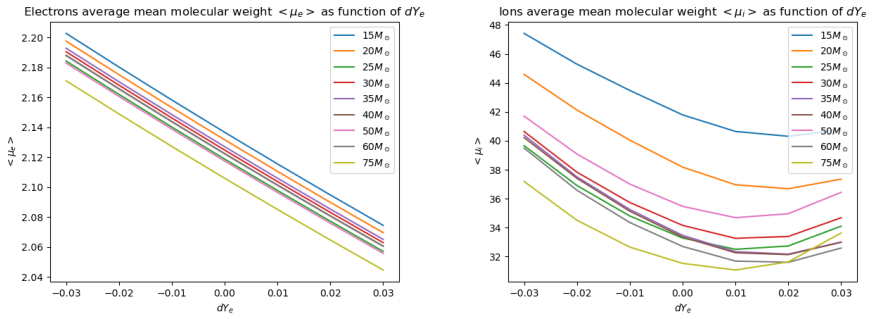

(a) (b)

Figure 5.8: Average mean molecular weights per electron, $\langle \mu_e \rangle$, and per ion, $\langle \mu_i \rangle$, as a function of electron fraction variation dY_e for all the stellar tracks.

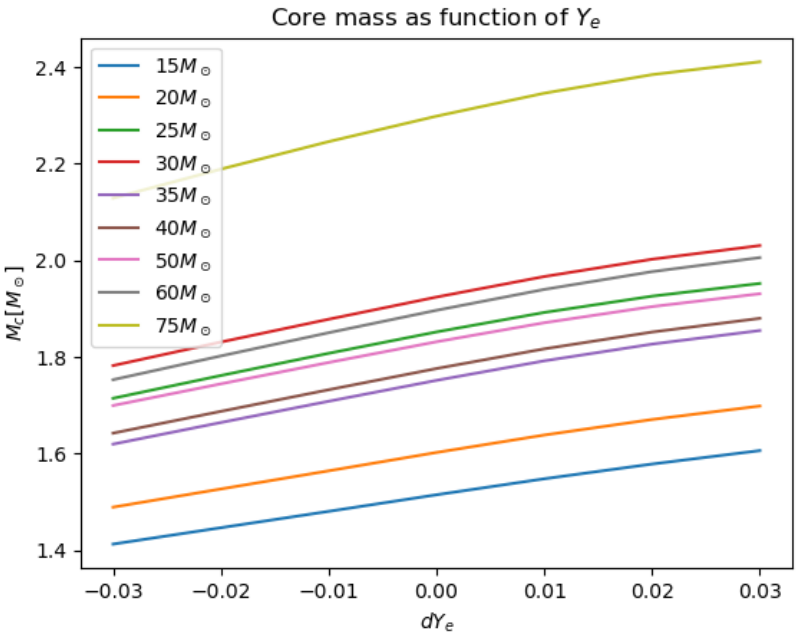

Figure 5.9: Predicted values of core's mass M_c as function of dY_e for all stellar models.

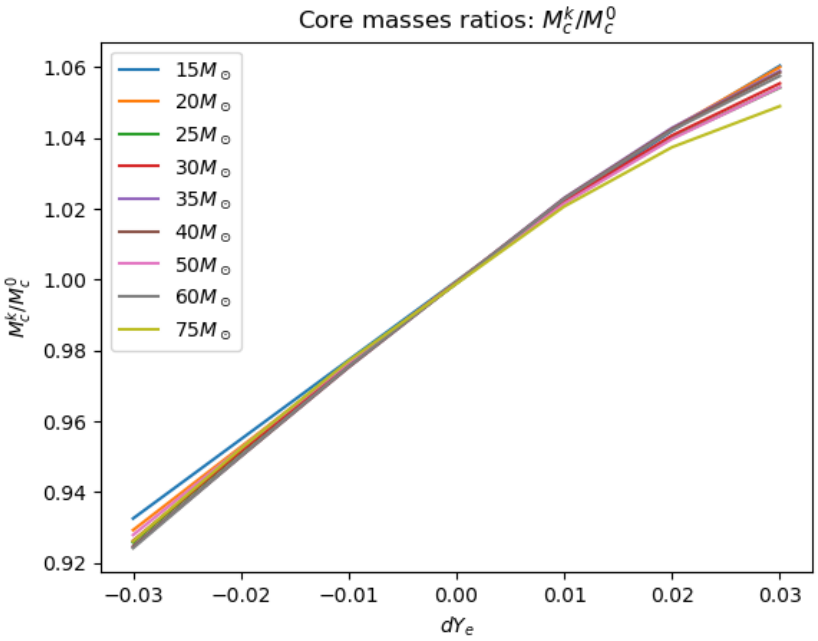

Figure 5.10: Ratios of M_c as a function of dY_e for all stellar models.

k	$\langle\mu^k\rangle$	$\langle\mu_e^k\rangle$	$\langle\mu_i^k\rangle$	$\langle\mu^k\rangle/\langle\mu^0\rangle$	M_c^k/M_c^0	M_c^k
−0.03	2.1049	2.2027	47.4205	1.0355	0.9325	1.4123
−0.02	2.0801	2.1802	45.2949	1.0233	0.9549	1.4461
−0.01	2.0561	2.1582	43.4808	1.0115	0.9773	1.4801
0.00	2.0327	2.1366	41.7906	1	1	1.5144
+0.01	2.0108	2.1154	40.6475	0.9892	1.0219	1.5476
+0.02	1.9912	2.0947	40.3122	0.9796	1.0421	1.5781
+0.03	1.9739	2.0744	40.7611	0.9711	1.0604	1.6059

Table 5.4: Mean molecular weights, core mass ratios and predicted core masses for the $15M_\odot$ stellar model as a function of Y_e. First column: k as defined in Sec. 4.3, such that the quantities listed in table are computed with $Y_e^k = Y_e^0 + kY_e^0$, where Y_e^0 is the electron fraction value computed with `MESA`. Second column: average mean molecular weight $\langle\mu^k\rangle$. Third column: average mean molecular weight per electron $\langle\mu_e^k\rangle$. Fourth column: average mean molecular weight per ion $\langle\mu_i^k\rangle$. Fifth column: $\langle\mu^k\rangle/\langle\mu^0\rangle$ ratios, as defined in Fig. 5.7. Sixth column: M_c^k/M_c^0 ratios, where M_c^0 is the mass of the core predicted with Y_e^0 and M_c^k is the mass predicted with Y_e^k. Seventh column: core mass M_c^k.

Chapter 6

Discussion

In the present thesis I attempted an exploration of the impact on the evolution of massive stars of possible quantitative uncertainties on Y_e, assuming them to be of order $\sim 1\%$. I have made no assumptions on the specific source of such uncertainties, but I noted that it can arise from conceptual assumptions ([Arcones et al., 2010]) or the details of a code's implementation ([Renzo et al., 2024]). With respect to this, it is worth noting that we find fluctuations of Y_e at a comparable level as displayed in Fig. 6.1. The latter shows the value of Y_e as a function of initial mass of the models at several evolutionary times as explained in Ch. 4. In multiple instances we find irregular changes of few percent between neighboring values of initial mass, suggesting a numerical rather than physical effect. In order to verify this, I refined the determination of these evolutionary times by interpolating to the same exact value fractional abundance ($X_j = 10^{-3}$) for all tracks and all selected isotopes. This resulted in minimal reduction of such fluctuations, supporting the hypothesis of their numerical origin.

It is reasonable to assume that these are similar to the deviations highlighted by Renzo et al. [2024], who advocate for always employing extensive nuclear reaction networks to simulate realistic pre-supernova evolution, especially for the purpose of chemical abundance studies. In contrast, to keep the computation manageable, I enabled simplifying assumptions for the `MESA` evolutionary tracks. This approach, while necessary, is also likely at the origin of the discrepancies seen in the comparison with the abundances predicted by `MESA` and `public_nse` in the present study (see Figs. 4.2 and 4.3). Indeed, I have validated the output of `public_nse` with a third independent code (`pynucastro`), and the compatibility between them has been thoroughly addressed by Smith et al. [2023]. In the preceding sections I have also repeatedly checked the validity of the NSE assumption, finding it to be well verified. The possibility that the discrepancy can be attributed to `MESA` is further supported by the recent analysis performed by its authors ([Jermyn et al., 2023]), who have highlighted possible deviations in terms of chemical abundances caused by the adoption of the `operator split` network approach, as opposed to a fully coupled hydrodynamic nuclear network, much more computationally intensive. However, the

adoption of a simplified treatment of nuclear processes does not impact significantly the structural properties of the star, as they are controlled by the energetics of the reactions, which can be described by taking into account only the main reactions rather than a complete network. I also note that in order to compute the evolutionary models, I have assumed zero rotation and no mass loss, which are somewhat unrealistic conditions, especially for massive stars. These assumptions are justified by the fact that these processes have marginal effects on the physical conditions in the stellar core ([see for instance Farmer et al., 2016]).

The results of my analysis indicate that a $\sim 1\%$ uncertainty on Y_e can have an important impact on stellar evolution. Taking ^{56}Ni as representative isotope of the late evolutionary stages of massive stars, I found uncertainties possibly larger than 100% in terms of chemical abundances. Whether these uncertainties have an actual impact on stellar evolution is difficult to determine, primarily because we expect the chemical profile to be largely erased upon core collapse. Indeed, a large fraction of the core ends up in the compact remnant, so its composition is almost completely altered (in the case of a neutron star) or becomes inconsequential (if a black hole is formed). The remaining material undergoes explosive nucleosynthesis, the products of which are certainly determined by the preceding composition, but in a highly uncertain way ([Janka, 2024]). In other words, chemical abundances are somewhat impractical to assess the possible effects on Y_e.

Therefore, I addressed the potential impact on structural core properties, taking the core mass as a proxy. Detailed studies of this aspect would require tailoring the Y_e uncertainty directly into the adopted stellar evolution code, as well as running simulations as accurate as possible in terms of nuclear reaction networks. As already explained, this is beyond the scope of the present study. Instead, I decide to adopt a simplified framework, probing the effect of Y_e on the core mass via the change in mean molecular weight, and found a possible error of order $\pm 5\%$ resulting from a $\pm 3\%$ uncertainty on Y_e, depending on the total stellar mass. This result relies a number of assumptions, namely:

- that stellar cores with altered Y_e are homologous to each other;
- that the conditions inside them are such that the use of an equation of state of an ideal gas plus radiation is appropriate;
- that cores to be compared this way have the same thermal stratification (more precisely, the same profile of β);
- that we can account a non homogeneus chemical profile in the core by means of a mass averaged mean molecular weight.

These assumptions are probably not completely verified, especially the last one. Therefore, the core mass uncertainties I found are probably to be taken as limiting values, or as indicative values in any case. Nonetheless, the analysis of the specific contribution from the μ_e and μ_i terms highlights the importance of accurate knowledge of Y_e for controlling the impact of NSE reactions on the

core mass. In this sense, the uncertainty on Y_e can have an important impact on the final fate of a massive star by affecting the compactness of the core, which is a critical parameter for explodability criteria ([O'Connor and Ott, 2011], [Ertl et al., 2016]). In particular, from a qualitative standpoint, my results indicate that a positive uncertainty on Y_e is reflected by a higher core mass and hence a more compact core, which is expected to disfavor the supernova explosion. These preliminary results need to be verified by more detailed investigations. In particular, a matter of uncertainty that is out of reach of the methods I employed concerns the details of the explosion-powering neutrino transport, which is certainly affected by lepton abundances and therefore by Y_e, and in principle could counterbalance the uncertainty on the core mass in terms explosion mechanism.

An additional remark should be made regarding the Chandrasekhar mass M_{Ch}, defined as $M_{Ch} = 5.86\,\mu_e^{-2}\,M_\odot$ (Iliadis [2015], see Sec. 2.4 for details). It can be seen from Eq. 4.7 and Fig. 5.9, describing how the mass of the core M_c changes as function of μ, that the functional form of the two relations is very similar: as Y_e increases, both M_{Ch} and M_c increase. On the one hand, this behavior suggests that the growth of M_c caused by Y_e could be balanced by a corresponding growth of M_{Ch}, possibly canceling the effect of Y_e. On the other hand, M_c depends also on μ_i that in turn depends on the reaction equilibria during NSE conditions [e.g. Fig. 5.8b, Seitenzahl et al., 2008]. Therefore, it is the very effect of an uncertainty on Y_e on the reaction equilibria that might result in uncertainties concerning the exact condition for instability, with a potential dependence on the total mass through $\langle\mu_i\rangle$. Taking into account that this reasoning involves approximations through the use of the core-averaged value $\langle\mu\rangle$, the details of how the uncertainty propagates to the stability criterion would require a more in depth study, properly accounting for shifts of Y_e during evolutionary calculations.

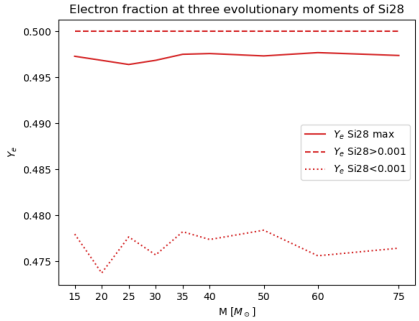

(a) Y_e at Si28 evolutionary moments

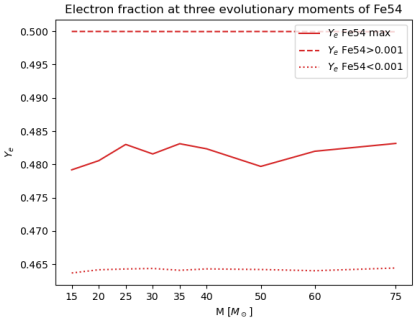

(b) Y_e at Fe54 evolutionary moments

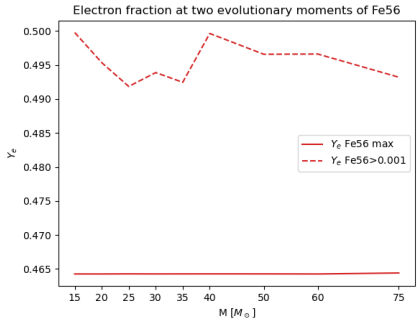

(c) Y_e at Fe56 evolutionary moments

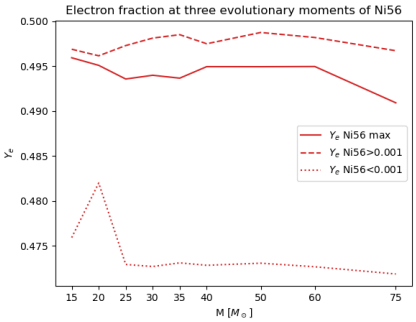

(d) Y_e at Ni56 evolutionary moments

Figure 6.1: Central electron fraction Y_e as a function of the initial mass of the stellar models, computed at the evolutionary instants described at the end of Sec. 4.1 for ^{28}Si, ^{54}Fe, ^{56}Fe and ^{56}Ni. Solid line: central Y_e at the evolutionary instant corresponding to the maximum abundance of the isotope. Dashed line: central Y_e when the isotope is starting to be synthesized in the center of the core. Dotted line: central Y_e when the isotope is depleted in the center of the core.

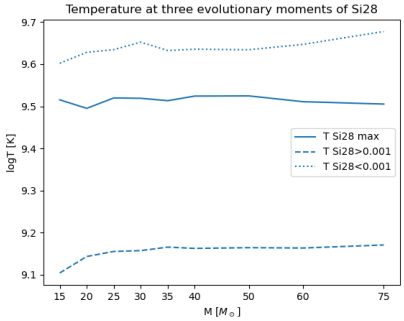

(a) T at Si28 evolutionary moments

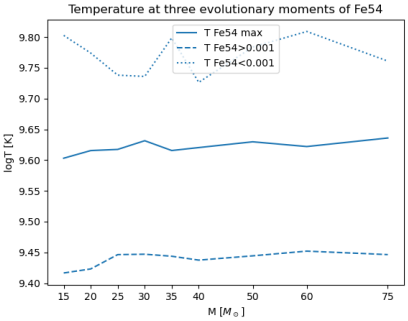

(b) T at Fe54 evolutionary moments

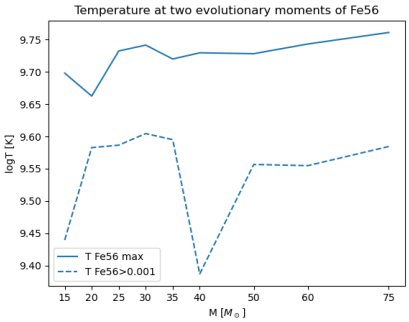

(c) T at Fe56 evolutionary moments

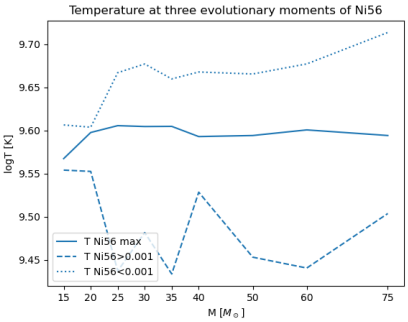

(d) T at Ni56 evolutionary moments

Figure 6.2: As in Fig. 6.1, but for temperature T.

Chapter 7

Conclusions

The simulations I performed with `star` resulted in a series of stellar tracks from which I gathered the information on temperature T, density ρ and electron fraction Y_e needed to compute the abundances at nuclear statistical equilibrium (NSE) in the iron core, for which I used another more flexible code, "`public_nse`". With the methods presented in Ch. 4 I was able to determine the total mass of ^{56}Ni in the stellar core and the predicted mass of the core itself, both as a function of the assumed uncertainty on Y_e. At the end of this thesis, we can draw the following conclusions:

1. The value of Y_e have an important effect on the abundances at NSE, that we traced in terms of the representative isotope ^{56}Ni. Over the explored range of uncertainty of Y_e, the core ^{56}Ni abundance changes by more than 100%, from a negligible amounts up to $15-20$% of the core mass. A comparable effect can be expected for other important nuclides, suggesting a relevant impact on the pre-supernova composition of the innermost layers, some of which could take part in explosive nucleosynthesis, depending on the explosion mass-cut.

2. An uncertainty of ± 3% on Y_e produces a variation of order ± 5% on the predicted core mass. This sizable effect is mostly due to the dependence of μ on μ_e and, hence, directly on Y_e, but there is an additional component that must be ascribed to μ_i. This latter depends on the altered reaction equilibria resulting from even a small change in Y_e. As a result, this effect is sensitive to thermodynamic conditions in the center and hence to the initial mass of the star. Therefore, this study suggests an effect on the core mass and hence its compactness, a parameter that is known to be critical to determine the explodability of the star and the mass cut.

3. Under the assumption of homology, we have linked the core mass with the mass averaged mean molecular weight as $M_c \propto \langle\mu\rangle^{-2}$. Given that $\langle\mu\rangle$ is largely controlled by μ_e, this dependence is similar to that characterizing the Chandrasekhar limiting mass, which is related to the condition for

collapse and stability. Under the assumptions made, these effects would cancel out making especially important the role of μ_i and the details of Y_e uncertainties on reaction equilibria.

Given the exploratory nature of this work, I adopted a number of simplifying assumptions that allowed me to highlight the main features of the functional dependencies of key parameters on the Y_e uncertainty, and to quantify its order-of-magnitude impact. The results I found, however, need to be verified on more rigorous grounds, for instance by testing how a shift on Y_e affects the evolution of massive stars once directly incorporated in the code and calculations. In order to do so, one must make sure that an accurate description of the nuclear reaction network is adopted, possibly coupled with hydrodynamics, a task that is expected to be very computationally intensive.

I did not attempt any comparison with observations for my results concerning chemical composition, although in principle a signature could be detected, for instance, by spectroscopic analysis of supernovae and supernova remnants. However, as I limited this investigation to the iron core, the material affected by Y_e is largely destined to end up in the compact remnant. Therefore, the effect of this uncertainty on the ejected material and the supernova light curves is not clear and to address this topic with satisfactory detail more refined methods are needed, such as hydrodynamical simulations, an accurate treatment of the explosive nucleosynthesis taking place during the supernova explosion and an assessment of the effect of Y_e uncertainties on neutrino transport.

Appendix A

Appendix

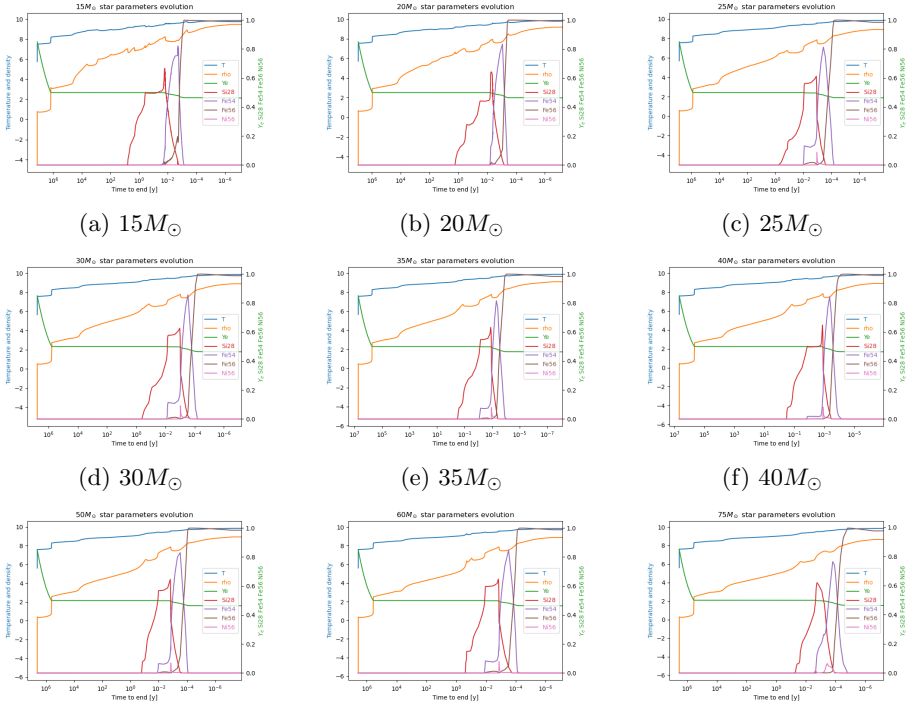

(a) $15M_{\odot}$ (b) $20M_{\odot}$ (c) $25M_{\odot}$

(d) $30M_{\odot}$ (e) $35M_{\odot}$ (f) $40M_{\odot}$

(g) $50M_{\odot}$ (h) $60M_{\odot}$ (i) $75M_{\odot}$

Figure A.1: Abundance evolution for the stellar tracks. Each panel shows a model with different initial mass. x-axis: the time to the end of the simulation in years. Left y-axis: logarithmic temperature and density scale. Right y-axis: electron fraction Y_e and abundances scale.

M [$M_\odot$]	15	20	25	30	35	40	50	60	75
$\log(T_{Si28,max}/K)$	9.51542	9.49516	9.51982	9.51908	9.51334	9.52430	9.52474	9.51100	9.50532
$\log(\rho_{Si28,max}/gcm^{-3})$	8.24563	7.86820	7.83069	7.76028	7.73693	7.80259	7.86320	7.85051	6.90456
$Y_{e,Si28,max}$	0.49730	0.49686	0.49641	0.49687	0.49752	0.49760	0.49734	0.49770	0.49739
$Si28_{max}$	0.66680	0.64257	0.61202	0.62615	0.63240	0.64782	0.64607	0.64797	0.62096
$\log(T_{Fe54,max}/K)$	9.60307	9.61548	9.61736	9.63148	9.61555	9.62036	9.62973	9.62201	9.63590
$\log(\rho_{Fe54,max}/gcm^{-3})$	7.89292	7.71137	7.49040	7.49351	7.44705	7.48990	7.57848	7.53996	7.34482
$Y_{e,Fe54,max}$	0.47917	0.48055	0.48299	0.48156	0.48310	0.48233	0.47969	0.48197	0.48315
$Fe54_{max}$	0.82142	0.83433	0.81349	0.85669	0.81609	0.84326	0.83013	0.84695	0.76514
$\log(T_{Fe56,max}/K)$	9.69806	9.66250	9.73233	9.74143	9.71992	9.72950	9.72815	9.74314	9.76101
$\log(\rho_{Fe56,max}/gcm^{-3})$	8.56926	8.36425	8.32683	8.36724	8.39263	8.42541	8.33039	8.36637	8.17390
$Y_{e,Fe56,max}$	0.46426	0.46426	0.46427	0.46426	0.46427	0.46427	0.46427	0.46426	0.46441
$Fe56_{max}$	0.99955	0.99974	0.99932	0.99916	0.99963	0.99952	0.99944	0.99911	0.99556
$\log(T_{Ni56,max}/K)$	9.56739	9.59764	9.60560	9.60456	9.60475	9.59292	9.59416	9.60065	9.59417
$\log(\rho_{Ni56,max}/gcm^{-3})$	8.10760	7.85129	7.78113	7.72380	7.64950	7.72431	7.77725	7.81030	7.33910
$Y_{e,Ni56,max}$	0.49594	0.49509	0.49357	0.49399	0.49367	0.49495	0.49494	0.49496	0.49092
$Ni56_{max}$	0.00514	0.01566	0.08715	0.09070	0.07953	0.08203	0.06885	0.07946	0.06520
$T_{Si28=10^{-3},1}$	9.10374	9.14292	9.15491	9.15686	9.16526	9.16219	9.16393	9.16311	9.17028
$\rho_{Si28=10^{-3},1}$	6.96968	6.62243	6.41166	6.23412	6.13933	6.04363	5.91820	5.77002	5.65682
$Y_{e,Si28=10^{-3},1}$	0.5	0.5	0.5	0.5	0.5	0.5	0.5	0.5	0.5
$Si28_{m1}$	1e-3	1e-3	1e-3	1e-3	1e-3	1e-3	1e-3	1e-3	1e-3
$T_{Fe54=10^{-3},1}$	9.41663	9.42319	9.44649	9.44713	9.44382	9.43751	9.44448	9.45213	9.44650
$\rho_{Fe54=10^{-3},1}$	8.00994	7.67670	6.86091	6.83930	6.91180	7.03899	6.87446	6.90211	6.47373
$Y_{e,Fe54=10^{-3},1}$	0.49998	0.49998	0.49998	0.49997	0.49997	0.49996	0.49997	0.49996	0.49994
$Fe54_{m1}$	1e-3	1e-3	1e-3	1e-3	1e-3	1e-3	1e-3	1e-3	1e-3
$T_{Fe56=10^{-3},1}$	9.43949	9.58262	9.58648	9.60443	9.59494	9.38694	9.55660	9.55472	9.58440
$\rho_{Fe56=10^{-3},1}$	8.11356	7.87569	7.57200	7.71332	7.56209	7.30534	7.87612	7.89134	7.39112
$Y_{e,Fe56=10^{-3},1}$	0.49979	0.49536	0.49185	0.49389	0.49246	0.49964	0.49659	0.49662	0.49321
$Fe56_{m1}$	1e-3	1e-3	1e-3	1e-3	1e-3	1e-3	1e-3	1e-3	1e-3
$T_{Ni56=10^{-3},1}$	9.55403	9.55254	9.43704	9.48160	9.43357	9.52841	9.45306	9.44045	9.50369
$\rho_{Ni56=10^{-3},1}$	8.19928	7.94841	7.30932	7.15486	7.24278	7.80595	7.24228	7.55215	7.08416
$Y_{e,Ni56=10^{-3},1}$	0.49688	0.49615	0.49729	0.49812	0.49850	0.49749	0.49875	0.49819	0.49672
$Ni56_{m1}$	1e-3	1e-3	1e-3	1e-3	1e-3	1e-3	1e-3	1e-3	1e-3
$T_{Si28=10^{-3},2}$	9.60243	9.62827	9.63472	9.65250	9.63264	9.63578	9.63445	9.64714	9.67790
$\rho_{Si28=10^{-3},2}$	7.88494	7.87997	7.59179	7.68666	7.54854	7.60163	7.62691	7.72420	7.58363
$Y_{e,Si28=10^{-3},2}$	0.47797	0.47374	0.47766	0.47571	0.47823	0.47738	0.47840	0.47561	0.47644
$Si28_{m2}$	1e-3	1e-3	1e-3	1e-3	1e-3	1e-3	1e-3	1e-3	1e-3
$T_{Fe54=10^{-3},2}$	9.80257	9.77388	9.73805	9.73589	9.79848	9.72627	9.78367	9.80895	9.76085
$\rho_{Fe54=10^{-3},2}$	9.16597	8.82791	8.37426	8.26163	8.73386	8.40824	8.60024	8.68089	8.17303
$Y_{e,Fe54=10^{-3},2}$	0.46367	0.46415	0.46427	0.46434	0.46407	0.46428	0.46419	0.46400	0.46441
$Fe54_{m2}$	1e-3	1e-3	1e-3	1e-3	1e-3	1e-3	1e-3	1e-3	1e-3
$T_{Ni56=10^{-3},2}$	9.60642	9.60377	9.66703	9.67708	9.65980	9.66781	9.66550	9.67720	9.71364
$\rho_{Ni56=10^{-3},2}$	7.91200	7.66496	7.85108	7.85746	7.81992	7.84926	7.86827	7.89530	7.81299
$Y_{e,Ni56=10^{-3},2}$	0.47592	0.48200	0.47293	0.47270	0.47311	0.47284	0.47308	0.47268	0.47187
$Ni56_{m2}$	1e-3	1e-3	1e-3	1e-3	1e-3	1e-3	1e-3	1e-3	1e-3

Table A.1: Physical parameters for all the stellar models presented in this work at the three evolutionary times described in Sec. 4.1. The subscripts 1 and 2 stand for the instant at which the nuclide is starting to be produced and the instant at which is depleted, respectively. The *max* subscript identifies the time at which the nuclide reaches the maximum abundance.

dY_e	$\langle\mu^k\rangle$	$\langle\mu_e^k\rangle$	$\langle\mu_i^k\rangle$	$\langle\mu^k\rangle/\langle\mu^0\rangle$	M_c^k/M_c^0	M_c^k
-0.03	2.0943	2.1975	44.5918	1.0374	0.9293	1.4887
-0.02	2.0683	2.1751	42.1267	1.0245	0.9528	1.5264
-0.01	2.0433	2.1531	40.0476	1.0121	0.9763	1.5640
0.00	2.0189	2.1315	38.1829	1	1	1.6021
$+0.01$	1.9965	2.1105	36.9660	0.9889	1.0225	1.6382
$+0.02$	1.9772	2.0898	36.6890	0.9793	1.0426	1.6704
$+0.03$	1.9609	2.0695	37.3530	0.9713	1.0601	1.6983

Table A.2: As in Tab. 5.4, but for the $20M_\odot$ stellar model.

dY_e	$\langle\mu^k\rangle$	$\langle\mu_e^k\rangle$	$\langle\mu_i^k\rangle$	$\langle\mu^k\rangle/\langle\mu^0\rangle$	M_c^k/M_c^k	M_c^k
−0.03	2.0702	2.1842	39.6645	1.0393	0.9258	1.7143
−0.02	2.0423	2.1619	36.9106	1.0253	0.9512	1.7615
−0.01	2.0161	2.1401	34.8077	1.0122	0.9761	1.8075
0.00	1.9919	2.1187	33.2852	1	1	1.8517
+0.01	1.9705	2.0977	32.5039	0.9893	1.0218	1.8921
+0.02	1.9532	2.0772	32.7356	0.9806	1.0400	1.9258
+0.03	1.9400	2.0570	34.1032	0.9739	1.0543	1.9522

Table A.3: As in Tab. 5.4, but for the $25M_\odot$ stellar model.

dY_e	$\langle\mu^k\rangle$	$\langle\mu_e^k\rangle$	$\langle\mu_i^k\rangle$	$\langle\mu^k\rangle/\langle\mu^0\rangle$	M_c^k/M_c^k	M_c^k
−0.03	2.0784	2.1904	40.6402	1.0391	0.9262	1.7821
−0.02	2.0506	2.1681	37.8325	1.0251	0.9516	1.8308
−0.01	2.0246	2.1462	35.7387	1.0122	0.9761	1.8781
0.00	2.0003	2.1247	34.1581	1	1	1.9240
+0.01	1.9785	2.1037	33.2634	0.9891	1.0221	1.9665
+0.02	1.9607	2.0831	33.3919	0.9802	1.0407	2.0023
+0.03	1.9470	2.0628	34.6843	0.9734	1.0555	2.0307

Table A.4: As in Tab. 5.4, but for the $30M_\odot$ stellar model.

dY_e	$\langle\mu^k\rangle$	$\langle\mu_e^k\rangle$	$\langle\mu_i^k\rangle$	$\langle\mu^k\rangle/\langle\mu^0\rangle$	M_c^k/M_c^k	M_c^k
−0.03	2.0798	2.1928	40.3869	1.0400	0.9246	1.6194
−0.02	2.0517	2.1704	37.5112	1.0259	0.95016	1.6641
−0.01	2.0251	2.1485	35.2569	1.0126	0.9753	1.7081
0.00	1.9999	2.1270	33.4713	1	1	1.7514
+0.01	1.9772	2.1059	32.3432	0.9886	1.0231	1.7919
+0.02	1.9583	2.0853	32.1708	0.9792	1.0429	1.8265
+0.03	1.9434	2.0650	33.0037	0.9718	1.0589	1.8547

Table A.5: As in Tab. 5.4, but for the $35M_\odot$ stellar model.

dY_e	$\langle\mu^k\rangle$	$\langle\mu_e^k\rangle$	$\langle\mu_i^k\rangle$	$\langle\mu^k\rangle/\langle\mu^0\rangle$	M_c^k/M_c^k	M_c^k
−0.03	2.0751	2.1880	40.2231	1.0400	0.9246	1.6421
−0.02	2.0472	2.1657	37.4090	1.0259	0.9501	1.6872
−0.01	2.0205	2.1438	35.1396	1.0126	0.9753	1.7320
0.00	1.9954	2.1223	33.3553	1	1	1.7759
+0.01	1.9729	2.1014	32.2680	0.9887	1.0230	1.8167
+0.02	1.9542	2.0808	32.1387	0.9794	1.0426	1.8515
+0.03	1.9394	2.0606	32.9941	0.9719	1.0586	1.8799

Table A.6: As in Tab. 5.4, but for the $40M_\odot$ stellar model.

dY_e	$\langle\mu^k\rangle$	$\langle\mu_e^k\rangle$	$\langle\mu_i^k\rangle$	$\langle\mu^k\rangle/\langle\mu^0\rangle$	M_c^k/M_c^k	M_c^k
−0.03	2.0743	2.1828	41.7038	1.0381	0.9279	1.6993
−0.02	2.0474	2.1606	39.0879	1.0247	0.9524	1.7442
−0.01	2.0219	2.1387	37.0112	1.0119	0.9766	1.7884
0.00	1.9981	2.1173	35.4712	1	1	1.8314
+0.01	1.9769	2.0964	34.6892	0.9894	1.0215	1.8707
+0.02	1.9595	2.0758	34.9643	0.9807	1.0398	1.9042
+0.03	1.9459	2.0557	36.4406	0.9739	1.0543	1.9309

Table A.7: As in Tab. 5.4, but for the $50M_\odot$ stellar model.

dY_e	$\langle\mu^k\rangle$	$\langle\mu_e^k\rangle$	$\langle\mu_i^k\rangle$	$\langle\mu^k\rangle/\langle\mu^0\rangle$	M_c^k/M_c^k	M_c^k
-0.03	2.0730	2.1878	39.4969	1.0402	0.9242	1.7528
-0.02	2.0445	2.1655	36.5851	1.0259	0.9501	1.8020
-0.01	2.0177	2.1436	34.3564	1.0125	0.9755	1.8501
0.00	1.9928	2.1222	32.7027	1	1	1.8966
$+0.01$	1.9705	2.1011	31.6903	0.9888	1.0228	1.9398
$+0.02$	1.9521	2.0805	31.6082	0.9795	1.0422	1.9767
$+0.03$	1.9378	2.0603	32.5909	0.9724	1.0576	2.0058

Table A.8: As in Tab. 5.4, but for the $60M_\odot$ stellar model.

dY_e	$\langle\mu^k\rangle$	$\langle\mu_e^k\rangle$	$\langle\mu_i^k\rangle$	$\langle\mu^k\rangle/\langle\mu^0\rangle$	M_c^k/M_c^k	M_c^k
-0.03	2.0513	2.1710	37.1901	1.0391	0.9261	2.1289
-0.02	2.0229	2.1489	34.5130	1.0247	0.9523	2.1890
-0.01	1.9971	2.1272	32.6582	1.0117	0.9771	2.2460
0.00	1.9740	2.1059	31.5331	1	1	2.2987
$+0.01$	1.9539	2.0850	31.0758	0.9898	1.0206	2.3463
$+0.02$	1.9381	2.0646	31.6374	0.9818	1.0374	2.3848
$+0.03$	1.9274	2.0445	33.6335	0.9764	1.0490	2.4114

Table A.9: As in Tab. 5.4, but for the $75M_\odot$ stellar model.

Bibliography

https://cococubed.com/code_pages/codes.shtml.

https://reaclib.jinaweb.org/index.php.

A. Arcones, G. Martínez-Pinedo, L. F. Roberts, and S. E. Woosley. Electron fraction constraints based on nuclear statistical equilibrium with beta equilibrium. , 522:A25, November 2010. doi: 10.1051/0004-6361/201014276.

G. Audi, A. H. Wapstra, and C. Thibault. The AME2003 atomic mass evaluation . (II). Tables, graphs and references. , 729(1):337–676, December 2003. doi: 10.1016/j.nuclphysa.2003.11.003.

Alessandro Chieffi, Marco Limongi, and Oscar Straniero. The Evolution of a 25 $M_{\odot}$ Star from the Main Sequence up to the Onset of the Iron Core Collapse. , 502(2):737–762, August 1998. doi: 10.1086/305921.

T. Ertl, H. Th. Janka, S. E. Woosley, T. Sukhbold, and M. Ugliano. A Two-parameter Criterion for Classifying the Explodability of Massive Stars by the Neutrino-driven Mechanism. , 818(2):124, February 2016. doi: 10.3847/0004-637X/818/2/124.

R. Farmer, C. E. Fields, I. Petermann, Luc Dessart, M. Cantiello, B. Paxton, and F. X. Timmes. On Variations Of Pre-supernova Model Properties. , 227 (2):22, December 2016. doi: 10.3847/1538-4365/227/2/22.

D. Hartmann, S. E. Woosley, and M. F. El Eid. Nucleosynthesis in Neutron-rich Supernova Ejecta. , 297:837, October 1985. doi: 10.1086/163580.

Christian Iliadis. *Nuclear physics of stars*. 2015. doi: 10.1002/9783527692668.

Hans-Thomas Janka. Explosion Mechanisms of Core-Collapse Supernovae. *Annual Review of Nuclear and Particle Science*, 62(1):407–451, November 2012. doi: 10.1146/annurev-nucl-102711-094901.

Hans-Thomas Janka. Core-collapse Supernova Theory: Status and Perspectives After 15 Years of 3D Modeling. In *EAS2024*, page 250, July 2024.

Adam S. Jermyn, Evan B. Bauer, Josiah Schwab, R. Farmer, Warrick H. Ball, Earl P. Bellinger, Aaron Dotter, Meridith Joyce, Pablo Marchant, Joey S. G. Mombarg, William M. Wolf, Tin Long Sunny Wong, Giulia C. Cinquegrana, Eoin Farrell, R. Smolec, Anne Thoul, Matteo Cantiello, Falk Herwig, Odette Toloza, Lars Bildsten, Richard H. D. Townsend, and F. X. Timmes. Modules for Experiments in Stellar Astrophysics (MESA): Time-dependent Convection, Energy Conservation, Automatic Differentiation, and Infrastructure. , 265(1):15, March 2023. doi: 10.3847/1538-4365/acae8d.

Rudolf Kippenhahn, Alfred Weigert, and Achim Weiss. *Stellar Structure and Evolution*. 2013. doi: 10.1007/978-3-642-30304-3.

P. Möller, J. R. Nix, W. D. Myers, and W. J. Swiatecki. Nuclear Ground-State Masses and Deformations. *Atomic Data and Nuclear Data Tables*, 59:185, January 1995. doi: 10.1006/adnd.1995.1002.

Evan O'Connor and Christian D. Ott. Black Hole Formation in Failing Core-Collapse Supernovae. , 730(2):70, April 2011. doi: 10.1088/0004-637X/730/2/70.

Evan P. O'Connor and Sean M. Couch. Exploring Fundamentally Three-dimensional Phenomena in High-fidelity Simulations of Core-collapse Supernovae. , 865(2):81, October 2018. doi: 10.3847/1538-4357/aadcf7.

Bill Paxton, Lars Bildsten, Aaron Dotter, Falk Herwig, Pierre Lesaffre, and Frank Timmes. Modules for Experiments in Stellar Astrophysics (MESA). , 192(1):3, January 2011. doi: 10.1088/0067-0049/192/1/3.

Bill Paxton, Matteo Cantiello, Phil Arras, Lars Bildsten, Edward F. Brown, Aaron Dotter, Christopher Mankovich, M. H. Montgomery, Dennis Stello, F. X. Timmes, and Richard Townsend. Modules for Experiments in Stellar Astrophysics (MESA): Planets, Oscillations, Rotation, and Massive Stars. , 208(1):4, September 2013. doi: 10.1088/0067-0049/208/1/4.

Bill Paxton, Pablo Marchant, Josiah Schwab, Evan B. Bauer, Lars Bildsten, Matteo Cantiello, Luc Dessart, R. Farmer, H. Hu, N. Langer, R. H. D. Townsend, Dean M. Townsley, and F. X. Timmes. Modules for Experiments in Stellar Astrophysics (MESA): Binaries, Pulsations, and Explosions. , 220(1):15, September 2015. doi: 10.1088/0067-0049/220/1/15.

Bill Paxton, Josiah Schwab, Evan B. Bauer, Lars Bildsten, Sergei Blinnikov, Paul Duffell, R. Farmer, Jared A. Goldberg, Pablo Marchant, Elena Sorokina, Anne Thoul, Richard H. D. Townsend, and F. X. Timmes. Modules for Experiments in Stellar Astrophysics (MESA): Convective Boundaries, Element Diffusion, and Massive Star Explosions. , 234(2):34, February 2018. doi: 10.3847/1538-4365/aaa5a8.

Bill Paxton, R. Smolec, Josiah Schwab, A. Gautschy, Lars Bildsten, Matteo Cantiello, Aaron Dotter, R. Farmer, Jared A. Goldberg, Adam S. Jermyn,

S. M. Kanbur, Pablo Marchant, Anne Thoul, Richard H. D. Townsend, William M. Wolf, Michael Zhang, and F. X. Timmes. Modules for Experiments in Stellar Astrophysics (MESA): Pulsating Variable Stars, Rotation, Convective Boundaries, and Energy Conservation. , 243(1):10, July 2019. doi: 10.3847/1538-4365/ab2241.

T. Rauscher. Nuclear Partition Functions at Temperatures Exceeding 10^{10} K. , 147(2):403–408, August 2003. doi: 10.1086/375733.

M. Renzo, J. A. Goldberg, A. Grichener, O. Gottlieb, and M. Cantiello. Progenitor Stars Calculated with Small Reaction Networks should not be Used as Initial Conditions for Core Collapse. *Research Notes of the American Astronomical Society*, 8(6):152, June 2024. doi: 10.3847/2515-5172/ad530e.

I. R. Seitenzahl, F. X. Timmes, A. Marin-Laflèche, E. Brown, G. Magkotsios, and J. Truran. Proton-rich Nuclear Statistical Equilibrium. , 685(2):L129, October 2008. doi: 10.1086/592501.

Alexander I. Smith, Eric T. Johnson, Zhi Chen, Kiran Eiden, Donald E. Willcox, Brendan Boyd, Lyra Cao, Christopher J. DeGrendele, and Michael Zingale. pynucastro: A Python Library for Nuclear Astrophysics. , 947(2):65, April 2023. doi: 10.3847/1538-4357/acbaff.

S. E. Woosley, A. Heger, and T. A. Weaver. The evolution and explosion of massive stars. *Reviews of Modern Physics*, 74(4):1015–1071, November 2002. doi: 10.1103/RevModPhys.74.1015.